



High-performance precious metal-free direct ammonia fuel cells endowed by Co-doped Ni_4Cu_1 anode catalysts

Zijun Hu^{a,1}, Song Lu^{b,1}, Fumin Tang^a, Daijun Yang^a, Cunman Zhang^a, Qiangfeng Xiao^{a,*}, Pingwen Ming^{a,*}

^a School of Automotive Studies & Clean Energy Automotive Engineering Center, Tongji University (Jiading Campus), 4800 Cao'an Road, Shanghai 201804, China

^b Department of Energy and Petroleum Engineering, University of Stavanger, 4036 Stavanger, Norway

ARTICLE INFO

Keywords:

Anion exchange membrane
Direct ammonia fuel cells
Ni-Cu-Co ternary catalyst
Ammonia oxidation reaction
DFT simulation

ABSTRACT

Anion exchange membrane-based direct ammonia fuel cells (AEM-DAFCs) have attracted increasing attention due to the advantages of ammonia. However, the high Pt loading in the anode substantially hampers the practical implementation of AEM-DAFCs. Herein, the $\text{Ni}_4\text{Cu}_1\text{Co}_x$ ($x = 0, 0.5, 1.0, 1.5$ and 2.0)-BP catalysts were prepared for the first time, achieving the best ammonia oxidation reaction (AOR) performance at $x = 1.5$. Density functional theory calculations reveal that such improvement is ascribed to the lowered adsorption energy and the Gibbs free energy of AOR intermediates as Co doping introduces electron aggregation around O atoms. The AEM-DAFC based on $\text{Ni}_4\text{Cu}_1\text{Co}_{1.5}$ -BP anode can deliver a peak power density (PPD) of 115.7 mW cm^{-2} and an open circuit voltage of 0.75 V at 80°C . According to our knowledge, such PPD is the highest among precious metal-free electrodes-based AEM-DAFCs, showing that the $\text{Ni}_4\text{Cu}_1\text{Co}_{1.5}$ -BP is a promising candidate for anode catalyst in AEM-DAFCs.

1. Introduction

The survival and development of human society are highly dependent on how to utilize energy. In 2021, fossil fuels supplied 80 % of the global energy demand, which resulted in significant emissions of carbon dioxide (CO_2) and other greenhouse gases into the atmosphere, causing serious consequences for the ecological environment [1–4]. The energy-related global CO_2 emissions grew to a record high (36.8 gigatonnes) in 2022, according to the latest data from the International Energy Agency (IEA) [5]. All nations' energy policies now generally favor low- or no-carbonization of their energy structures. Therefore, it is urgent to develop renewable energy and efficient clean combustion technologies that can replace fossil fuels. Hydrogen, a carbon-free, clean and efficient fuel, is considered an alternative to fossil fuels [6]. However, several challenges regarding the production, distribution, transportation and storage of hydrogen have limited its deployment and widespread use as a practical fuel [7]. Ammonia is another carbon-free fuel with attractive properties, such as high energy density (liquid ammonia, 12.9 MJ L^{-1}), easy liquefaction (-33.4°C at 0.1 MPa or 25°C at 0.9 MPa) and low cost [8–10]. Furthermore, ammonia has been

widely used in the synthesis of chemical fertilizers, explosives, plastics, fibers and other compounds since the development of the Haber-Bosch process in 1909 [11,12]. Therefore, the infrastructure and regulations for the production, storage, transport and use of ammonia have been established globally, making its development superior to that of other energy carriers [13,14]. The estimated world ammonia production in 2021 was 150 million metric tons with an expected growth of 4 % during the next 4 years [11]. Moreover, many countries have introduced the strategic layout of ammonia as the future energy development direction [15]. For example, the Japanese Ministry for Economy, Trade, and Industry (METI) updated the road map for fuel ammonia in February 2021, which includes ammonia demand, production, supply, application, etc [16]. In 2020, the US House of Representatives published draft legislation that explicitly defined ammonia as a “low-carbon fuel” for the first time [17]. The UK's Royal Society published an influential policy briefing on ammonia as a “zero-carbon fertiliser, fuel and energy store” and pointed out that ammonia was the lowest-cost method and the most technologically-ready option for transporting energy over long distances [18]. It is clear that the potential of ammonia for a carbon-free fuel future has been increasingly realized and is influencing national policy

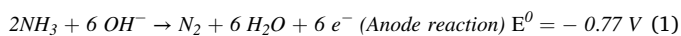
* Corresponding authors.

E-mail addresses: xiaoqf@tongji.edu.cn (Q. Xiao), pwm@tongji.edu.cn (P. Ming).

¹ These authors contributed equally to this work

regarding energy utilization.

Direct ammonia fuel cells (DAFCs), which directly convert chemical energy into electricity [19], are regarded as an important technology and solution in the utilization of ammonia fuel because they use ammonia as fuel to provide electricity while producing water and nitrogen, resulting in no pollution to the environment. Among DAFCs, low-temperature anion exchange membrane-based direct ammonia fuel cells (AEM-DAFCs) have attracted increasing attention from many researchers in recent years because of their advantages, such as small size, low-temperature operation and fast start-up, which are more suitable for mobile applications [20,21]. In AEM-DAFCs, ammonia is oxidized at the anode to form nitrogen, while oxygen is reduced to OH^- at the cathode, as shown below [22]:



Based on the above reaction, the anion exchange membrane was used in low-temperature DAFCs with a maximum power density of 16 mW cm^{-2} at 25°C by Lan and Tao for the first time in 2010 [22]. After that, the performance of AEM-DAFCs has been greatly improved due to the development and optimization of electrocatalysts as well as anion exchange membranes [23–27]. For instance, Gottesfeld et al. demonstrated an AEM (Tokuyama membrane, $30\text{ }\mu\text{m}$ thickness)-DAFC with a peak power density (PPD) of 280 mW cm^{-2} at 100°C , in which the PtIr/C was used as anode catalysts, the Ag-based as cathode catalyst and 12 M NH_3 in 2.5 M KOH as anode fuel [24]. Using a PtIrZn₂/SiO₂-CNTCOOH anode catalyst, Li et al. [25] prepared an AEM-DAFC which delivered a PPD of 314 mW cm^{-2} at 95°C . Wang et al. [27] achieved an AEM-DAFC with a PPD of 410 mW cm^{-2} when working with a 7 M NH_3 in 3 M KOH fuel solution at 110°C , employing the homemade AEM (PAP-TP-85, $13\text{ }\mu\text{m}$ thickness).

Obviously, great progress has been made in the performance of direct ammonia fuel cells in recent years. Pt-based materials have become the most common anode catalysts in AEM-DAFCs. However, the precious metal loadings in the anodes are excessively high, mostly ranging from 2 to $4\text{ mg}_{\text{PGM}}\text{ cm}^{-2}$ [9,24,27–30], whereas the total platinum (anodes and cathodes) loadings for most hydrogen fuel cells are only 0.4 – $0.5\text{ mg}_{\text{Pt}}\text{ cm}^{-2}$ [31]. The practical application of Pt-based catalysts in AEM-DAFCs has been limited by their high cost, scarce resources, and easy deactivation by N_{ads} [32,33]. Since AEM-DAFCs are operated in alkaline conditions, non-precious metal catalysts are alternatively feasible to achieve low-cost and high-performance AEM-DAFCs [34].

As a result, there have been some works of AEM-DAFCs using non-precious metal catalysts as anodes [22,35–37]. All the anode catalysts used in these reports are Ni-based materials. It is because the Ni-based materials have high ammonia oxidation reaction (AOR) activity in non-precious metal catalysts, as reported in previous work on ammonia electrooxidation [38–40]. Among them, the NiCu bimetallic catalyst, which was first reported to be used for the electrooxidation of ammonia in 2018 [41], has become the most representative Ni-based ammonia electrooxidation catalyst. This is due to the synergistic interaction between Ni and Cu, leading to its high ammonia electrooxidation activity and decent stability [42]. The combination of Ni and Cu helps them to form more oxyhydroxides, which are the active substances in the final AOR [43,44]. In addition, the doping of Cu^{2+} can form dangling bands with high electron density on $\text{O}_{\text{O-Ni}}$, which can promote the adsorption of NH_3 [45]. However, high Cu doping can decrease the active surface and deteriorate AOR activity. When the ratio of Ni:Cu is 4:1, the catalyst has the best AOR performance, as reported in the literature [43]. To further enhance the AOR activity of NiCu bimetal catalysts, Zhu et al. [45] first introduced Fe^{3+} with lower electronegativity to obtain a high electron density on $\text{O}_{\text{O-Ni}}$, resulting in a lower Gibbs free energy of NH_3 adsorption than $\text{Ni}_{(1-x)}\text{Cu}_x\text{OOH}$, and a better AOR performance. Similarly,

Zhang et al. [37] doped different concentrations of Fe into the Ni_4Cu_5 alloy to synthesize the ternary alloy catalysts that exhibited excellent activity and durability for both AOR and oxygen reduction reaction (ORR). And the first symmetric direct ammonia fuel cell was prepared with an open circuit voltage (OCV) of 0.62 V and a maximum current density of 67 mA cm^{-2} , thanks to the superior bifunctional activity of the $\text{Ni}_4\text{Cu}_5\text{Fe}_1/\text{C}$ catalyst.

Herein, we introduced different contents of Co into Ni_4Cu_1 catalyst to acquire $\text{Ni}_4\text{Cu}_1\text{Co}_x$ ($x = 0, 0.5, 1.0, 1.5$ and 2.0)-BP catalysts by a facile hydrothermal method. Co doping can significantly increase the oxidation activity of Ni toward ammonia [46], urea [47], methanol [48] and ethanol [49] due to the increased OH^- absorption and formation of CoOOH at a lower potential [46,50]. Our AOR test results indicated that Co doping could significantly improve the AOR activity of Ni_4Cu_1 catalyst. The optimized $\text{Ni}_4\text{Cu}_1\text{Co}_{1.5}$ -BP catalyst presented a higher AOR current and a lower onset potential compared to Ni_4Cu_1 -BP. Density functional theory calculations showed that Co atoms can promote electron aggregation around O atoms, lower the AOR intermediates' adsorption energy and the Gibbs free energy and in turn improve the AOR activity. Paired with our previously developed Mn-Co-BP2000 cathode [9], the $\text{Ni}_4\text{Cu}_1\text{Co}_{1.5}$ anode was assembled into precious metal-free AEM-DAFCs which exhibited a high PPD of 115.7 mW cm^{-2} with $7\text{ M NH}_3 + 3\text{ M KOH}$ as anode fuel at 80°C . According to our knowledge, this is also the highest PPD reported so far in AEM-DAFCs based on non-precious metal catalyst electrodes.

2. Experimental section

2.1. Materials

All chemical reagents were of analytical grade and used as received without further purification. Nickel(II) sulfate hexahydrate ($\text{NiSO}_4 \cdot 6\text{H}_2\text{O}$, $\geq 98.5\%$), Copper(II) sulfate pentahydrate ($\text{CuSO}_4 \cdot 5\text{H}_2\text{O}$, $\geq 99\%$), Cobalt(II) sulfate heptahydrate ($\text{CoSO}_4 \cdot 7\text{H}_2\text{O}$, $\geq 99.5\%$), Sodium borohydride (NaBH_4 , $\geq 96\%$), potassium hydroxide (KOH , $\geq 85\%$), ammonia aqueous ($\text{NH}_3 \cdot \text{H}_2\text{O}$, 25–28%) and isopropanol were purchased from Sinopharm Chemical Reagent Co., Ltd. The BP2000 was obtained from Cabot Corporation. The anion exchange ionomer solution (5 wt%) and alkaline polymer electrolyte membranes (AEM, $15\text{ }\mu\text{m}$, Alklymer W–211415) were gained from EVE Institute of New Energy Technology.

2.2. Preparation of catalysts

The carbon-supported $\text{Ni}_4\text{Cu}_1\text{Co}_x$ ($x = 0, 0.5, 1.0, 1.5$ and 2.0) catalysts were synthesized using a simple hydrothermal method [51]. Typically, 50 mg BP2000, a carbon support that had been functionalized by acid to introduce oxidized species for increasing the cations' adsorption activity according to the literature [9], was impregnated with 20 mL of DI water and ultrasonicated for 20 min . Afterward, properly proportioned $\text{NiSO}_4 \cdot 6\text{H}_2\text{O}$, $\text{CuSO}_4 \cdot 5\text{H}_2\text{O}$ and $\text{CoSO}_4 \cdot 7\text{H}_2\text{O}$ were added to the BP2000 suspension and ultrasonicated for another 20 min . The mixture was then placed in an ice-water bath. Subsequently, 20 mL ice-cold NaBH_4 (6 mmol) solution was added dropwise into the above solution under magnetic stirring. After stirring at 0°C for 2 h , the mixed aqueous solution was transferred to a 100 mL Teflon-lined stainless-steel autoclave for hydrothermal reaction at 150°C for 4 h . Then, the catalyst was collected by centrifugation at 9000 rpm for 10 min and washed five times with DI water before freeze-drying under a vacuum. In this experiment, the molar amount of metal cation in the precursor was 2 mmol with the molar ratio of Ni to Cu being 4:1. Finally, the catalysts with different molar ratios of Ni to Co were prepared by controlling the Co content in the precursor, varying the molar ratio of Ni to Co from 4:0–4:0.5, 4:1, 4:1.5 and 4:2. Accordingly, they were denoted as Ni_4Cu_1 -BP, $\text{Ni}_4\text{Cu}_1\text{Co}_{0.5}$ -BP, $\text{Ni}_4\text{Cu}_1\text{Co}_{1.0}$ -BP, $\text{Ni}_4\text{Cu}_1\text{Co}_{1.5}$ -BP, and $\text{Ni}_4\text{Cu}_1\text{Co}_{2.0}$ -BP, respectively. For Co-BP, only 2 mmol $\text{CoSO}_4 \cdot 7\text{H}_2\text{O}$ was

added to the BP2000 suspension for reaction while the other conditions were kept the same as those described above.

2.3. Characterization

Scanning transmission electron microscopy (STEM) imaging and energy-dispersive X-ray spectroscopy (EDS) mapping were observed on an FEI Talos F200X (USA) microscope coupled with a cold field emission gun operating at 200 kV. The field-emission scanning electron microscopy (FESEM) images and EDS spectra were carried out on the FEI Quanta 200FEG (USA) equipped with an energy-dispersive X-ray spectrometer at a high vacuum with an accelerating voltage of 20 kV. X-ray diffraction (XRD) patterns of samples were tested on an X-ray diffractometer (D2 PHASER, Bruker, Germany) using Cu K_α radiation ($\lambda = 0.154$ nm). The elemental compositions in catalysts were further detected by an inductively coupled plasma-optical emission spectroscopy (ICP-OES, Avio 500, Perkin Elmer, USA). The X-ray photoelectron spectra (XPS) measurements were examined by an X-ray photoelectron spectrometer (ESCALAB 250Xi, Thermo Scientific, USA) by using an Al $K\alpha$ source ($h\nu = 1486.6$ eV, 650 μm of beam spot).

2.4. Electrochemical measurements

All the electrochemical measurements were carried out via an electrochemical workstation (CHI 760E, CH Instruments, Chenhua Instrument Co., China) with a rotating disk electrode (RDE, Pine Research Instruments) in a typical three-electrode system. Specifically, the catalyst-supported glassy carbon disk (Model AFMSRCE, 5 mm diameter, Pine), a graphite rod and a double-salt-bridge Hg/HgO electrode (1.0 M KOH) were used as the working, counter and reference electrodes, respectively. The catalyst ink was prepared by dispersing 5 mg catalyst in 980 μL isopropanol and 20 μL anion exchange ionomer solution, followed by sonication for 1 h. Then, 20 μL of catalyst ink was drop-coated onto the clear glassy carbon disk and allowed to dry at ambient temperature to yield a thin-film electrode, resulting in an approximate catalyst loading of 0.51 mg cm^{-2} . All the solutions were Ar-saturated for electrochemical testing. Cyclic voltammograms (CV) of AOR were all recorded at a range of $-0.1 \sim 0.8$ V vs. Hg/HgO with a scan rate of 50 mV s^{-1} unless otherwise stated. The electrochemical active surface areas (ECSA) of the $\text{Ni}_4\text{Cu}_1\text{-BP}$ and $\text{Ni}_4\text{Cu}_1\text{Co}_{1.5}\text{-BP}$ were estimated by measuring the electrochemical capacitance of the electrode-electrolyte interface in the non-Faradaic section double-layer capacitance (C_{dl}) range of the voltammograms. Using 1 M KOH as the electrolyte, the electrode was cycled between 0.05 V and 0.15 V vs. Hg/HgO, at scan rates between 10 mV s^{-1} and 100 mV s^{-1} until the obtained voltammograms were stabilized. To determine the measured capacitance, the average of the positive and negative capacitance currents at the center of the potential window was plotted versus the scan rate [52]. Linear sweep voltammetry (LSV) curves were performed in Ar-saturated 0.1 M $\text{NH}_3 + 1$ M KOH electrolyte by sweeping the potential from $-0.1 \sim 0.8$ V vs. Hg/HgO at a scan rate of 10 mV s^{-1} with varying rotating speeds from 400 to 1600 rpm. For the experiments of investigating temperature effects, NH_3 concentration effects and KOH concentration effects, a fresh electrode and a fresh ammonia electrolyte were used for every single measurement to ensure the accuracy of the experiments. The chronoamperometry (CA) tests were measured in the Ar-saturated electrolyte at 0.65 V vs. Hg/HgO. Before all the electrochemical experiments, the catalyst working electrodes were first activated by CV cycles ($-0.1 \sim 0.8$ V vs. Hg/HgO) in freshly Ar-saturated different concentration KOH electrolyte at a scan rate of 50 mV s^{-1} . And the KOH concentration in the electrolyte used for activation was consistent with that of the electrolyte for AOR performance tested later.

2.5. Density functional theory (DFT) calculations

Spin-polarized calculations (the geometry relaxation and electronic

properties) were carried out by using VASP software [53,54]. The Perdew-Burke-Ernzerh (PBE) function within the generalized gradient approximation (GGA) and norm-conserving pseudopotentials were used to describe the electron exchange-correlation interaction [55–57]. The Van der Waals force and long-range interactions were included by using the DFT-D3 method developed by Grimme [58,59]. The energy cutoff of electron wave functions was set to 500 eV and a k-point sampling of $6 \times 6 \times 1$ (structure relaxation) and $8 \times 8 \times 1$ (electronic structure calculations) for all systems were tested to achieve convergence. The convergence criterion for energy and force was set to 1.0×10^{-5} eV and 1.0×10^{-2} eV/Å, respectively. Based on the computational hydrogen electrode (CHE) [58], the Gibbs free energy changes (ΔG) were calculated by the Equation below:

$$\Delta G = \Delta E + \Delta E(\text{ZPE}) - T\Delta S \quad (4)$$

where the ΔE , $\Delta E(\text{ZPE})$ and ΔS are the adsorption energy of intermediates, the change in zero-point energy and entropy contribution, respectively. T was set to be 298.15 K.

2.6. Single-cell tests

The procedure for assembling DAFC was similar to our previous study [9]. Specifically, the anode catalyst ink was prepared by mixing the anode catalysts ($\text{Ni}_4\text{Cu}_1\text{-BP}$, $\text{Ni}_4\text{Cu}_1\text{Co}_{0.5}\text{-BP}$, $\text{Ni}_4\text{Cu}_1\text{Co}_{1.0}\text{-BP}$, $\text{Ni}_4\text{Cu}_1\text{Co}_{1.5}\text{-BP}$, or $\text{Ni}_4\text{Cu}_1\text{Co}_{2.0}\text{-BP}$), 5 wt% anion exchange ionomer solution, and isopropanol under ultrasonication for 1 h in an ice-water bath. The cathode catalyst ink was prepared by mixing Mn-Co-BP2000 (home-made cathode catalyst [9]), 5 wt% Nafion solution (The Chemours Chemical Co., Ltd.), and isopropanol under ultrasonication for 1 h in an ice-water bath. Both the mass ratios of the anode and cathode catalysts to their corresponding pure ionomers were 3:1. The anode catalyst inks and the cathode catalyst inks were then respectively sprayed onto a carbon cloth (W0S1009, Ce Tech Co., Ltd, Taiwan) and a carbon paper (28BC, SGL Carbon, Wiesbaden, Germany) and dried at 80 °C. The catalyst loadings were controlled as 10 mg cm^{-2} for the anode and 1.5 mg cm^{-2} for the cathode. Afterward, the MEAs with an active area of 2.25 cm^2 were assembled by an anode electrode, an AEM and a cathode electrode. The AEM was first immersed in 2 M KOH solution at 60 °C for 12 h to replace the Cl^- anion with OH^- , and then was washed three times with DI water before it was pressed between the anode and cathode electrodes. Anode fuels, 3 M KOH solutions with x M NH_3 ($x = 3, 5, 7$ and 9), were controlled by a peristaltic pump and flowed into the anode flow field at 5 mL min^{-1} , while pure O_2 with 50 % relative humidity and 200 kPa backpressure entered the cathode flow field at 200 mL min^{-1} under the control of a fuel cell test station (G20, Greenlight Innovation Corp., Canada). AEM-DAFCs were operated at 80 °C and their polarization curves were recorded by a Gamry electrochemical instrument (Reference 3000, Gamry Instruments, Inc., USA). Before the AEM-DAFCs test, 3 M KOH was used as anode fuel to activate the anode electrodes in the three-electrode system. In this process, the anode electrodes were electrochemically activated continuously for 10 times by linear sweeping from $-0.1 \sim 0.8$ V vs. Hg/HgO at a scan rate of 10 mV s^{-1} .

3. Results and discussion

3.1. Characterization of the synthesized samples

The XRD patterns of the as-synthesized $\text{Ni}_4\text{Cu}_1\text{Co}_x$ ($x = 0, 0.5, 1.0, 1.5$ and 2.0) are shown in Fig. 1a. It can be seen that all the samples exhibit diffraction peaks at nearly 44.47° and 51.81° corresponding to the (111) and (200) planes of Ni, with the space group of $Fm\text{-}3m$ ($a=b=c=3.524$ Å, JCPDS No. 04–0850). Meanwhile, the diffraction peaks at 43.51° and 50.74° correspond to the (111) and (200) planes of Cu ($a=b=c=3.615$ Å, $Fm\text{-}3m$, JCPDS No. 04–0836) in $\text{Ni}_4\text{Cu}_1\text{-BP}$. The

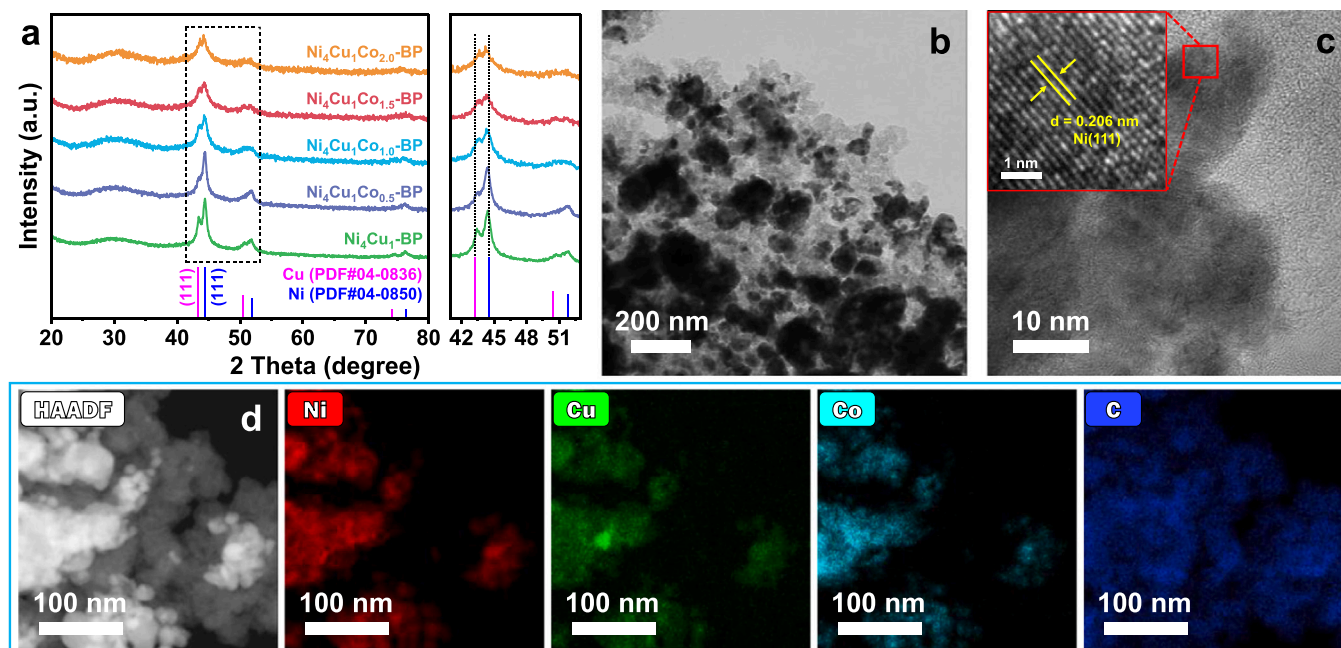


Fig. 1. (a) XRD patterns of $\text{Ni}_4\text{Cu}_1\text{BP}$, $\text{Ni}_4\text{Cu}_1\text{Co}_{0.5}\text{BP}$, $\text{Ni}_4\text{Cu}_1\text{Co}_{1.0}\text{BP}$, $\text{Ni}_4\text{Cu}_1\text{Co}_{1.5}\text{BP}$ and $\text{Ni}_4\text{Cu}_1\text{Co}_{2.0}\text{BP}$, (b) TEM image of $\text{Ni}_4\text{Cu}_1\text{Co}_{1.5}\text{BP}$, (c) HRTEM image (inset: lattice fringes pattern) of $\text{Ni}_4\text{Cu}_1\text{Co}_{1.5}\text{BP}$, (d) HAADF-STEM image of $\text{Ni}_4\text{Cu}_1\text{Co}_{1.5}\text{BP}$ and the corresponding EDS elemental mappings of Ni, Cu, Co and C.

magnified XRD spectra in the range of 41° to 52° show that the (111) plane peak position of Ni tends to shift toward lower 2θ angles with increasing Co doping concentration while the (111) plane peak position of Cu tends to shift toward higher 2θ angles, corresponding to the expansion and contraction of the interlayer spacing, respectively, resulting from the cell parameters of Co ($a=b=c=3.545 \text{ \AA}$, $Fm-3$, JCPDS No. 15–0806) are larger than Ni but smaller than Cu [45,60]. In

addition, as the concentration of Co doping increases, the crystallinity of the samples decreased because Co phase has a relatively lower crystallinity (Fig. S1a) than Cu and Ni phases.

As shown in the TEM picture (Fig. 1b), the irregularly shaped $\text{Ni}_4\text{Cu}_1\text{Co}_{1.5}$ nanoparticles are distributed on the surface of the pre-treated BP2000 sample similar to the $\text{Ni}_4\text{Cu}_1\text{BP}$ sample (Fig. S1b). The high-resolution TEM (HRTEM, Fig. 1c) image reveals that the interlayer

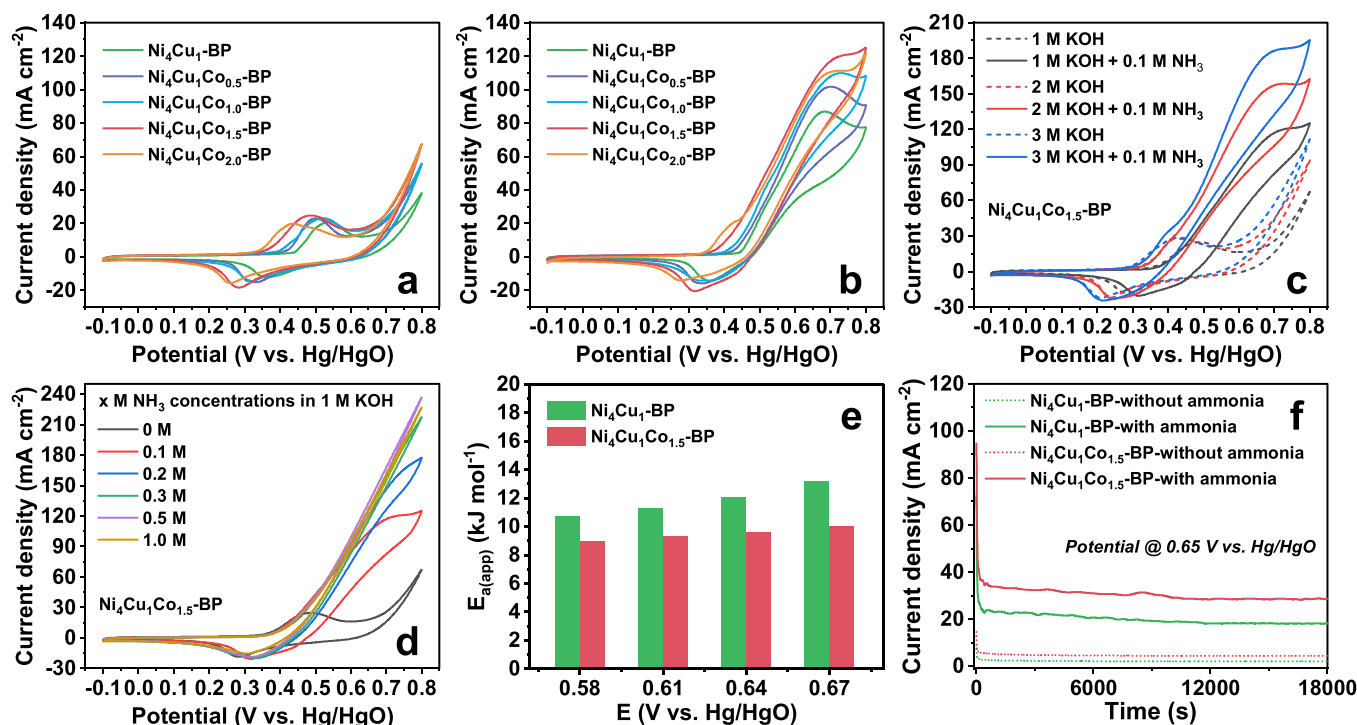
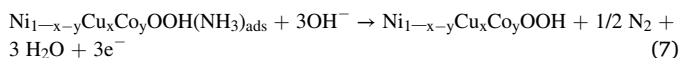
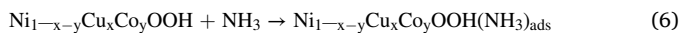
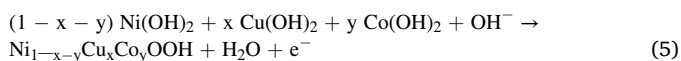


Fig. 2. (a) CV curves of all the samples in (a) 1 M KOH electrolyte and (b) 1 M KOH electrolyte with 0.1 M NH_3 , (c) CV curves of $\text{Ni}_4\text{Cu}_1\text{Co}_{1.5}\text{BP}$ in 0.1 M NH_3 electrolyte with different concentrations of KOH, (d) CV curves of $\text{Ni}_4\text{Cu}_1\text{Co}_{1.5}\text{BP}$ in 1 M KOH electrolyte with different concentrations of NH_3 , (e) The apparent activation energy (E_a) comparison of $\text{Ni}_4\text{Cu}_1\text{BP}$ and $\text{Ni}_4\text{Cu}_1\text{Co}_{1.5}\text{BP}$ in 1 M KOH electrolyte with 0.1 M NH_3 at various potentials vs. Hg/HgO, (f) Chronoamperograms curves of $\text{Ni}_4\text{Cu}_1\text{BP}$ and $\text{Ni}_4\text{Cu}_1\text{Co}_{1.5}\text{BP}$ at 0.65 V vs. Hg/HgO in 1 M KOH electrolyte with and without 0.1 M NH_3 .

spacing for Ni₄Cu₁Co_{1.5}-BP is 0.206 nm, which can be assigned to the (111) crystal plane of Ni, in accordance with the XRD results. Fig. 1d presents that the Ni, Cu and Co elements are uniformly distributed within the nanoparticles, confirming the formation of Ni-Cu-Co ternary nanoparticles on BP2000. Similar results are also observed for the as-prepared Ni₄Cu₁-BP, as shown in Fig. S1c and d. Moreover, to understand the metal elemental compositions in the synthesized samples, the EDS and ICP-OES analyses were applied to the Ni₄Cu₁Co_x (x = 0, 0.5, 1.0, 1.5 and 2.0)-BP, as shown in Fig. S2 and Table S1, respectively. The results exhibit that the metal elemental ratios in the Ni₄Cu₁Co_x (x = 0, 0.5, 1.0, 1.5 and 2.0)-BP are similar to the experimental design.

3.2. Evaluation of ammonia oxidation reaction

Electrochemical measurements were conducted to further characterize the AOR activity of the as-synthesized Ni₄Cu₁Co_x (x = 0, 0.5, 1.0, 1.5 and 2.0)-BP under different operation conditions. Fig. 2a presents cyclic voltammograms recorded on the samples in 1 M KOH electrolyte. A pair of similar redox peaks appear in the anodic and cathodic regions of all the samples, which were mainly attributed to the reversible reaction between M²⁺/M³⁺ (M=Ni, Cu or Co) in the alkaline situation [61, 62]. As shown in Fig. 2b, all the samples display good AOR performance, resulting in a very significant anodic current density. Based on the mechanism of AOR on Ni-based catalysts [43,63]:



A direct electron transfer from the adsorbed NH₃ to the Ni_{1-x-y}Cu_xCo_yOOH was considered in the AOR. Moreover, the Ni_{1-x-y}Cu_xCo_yOOH was the real activated substance, which was further confirmed by the results in Fig. S3a–e that all the AOR happened after the formation of Ni₄Cu₁Co_x (x = 0, 0.5, 1.0, 1.5 and 2.0)-OOH. Besides, all the Co-doped Ni₄Cu₁-BP samples showed higher AOR current densities than Ni₄Cu₁-BP and the highest one was obtained on the Ni₄Cu₁Co_{1.5}-BP. It may be because the doping of Co can increase the absorption of OH[−], promoting reactions (5) and (7) [46]. It can be clearly shown in Fig. S4 that with the increase of Co doping amount, the AOR onset potential (estimated here from the tangent method [64,65]) of the catalysts decreased continuously, but the AOR current density first increased and then decreased with a maximum anodic current density of 104.08 mA cm^{−2} at 0.65 V vs. Hg/HgO in Ni₄Cu₁Co_{1.5}-BP. Because according to EDS and ICP-OES results, the increase of Co content would reduce the Ni and Cu contents, and Co could not be used as a standalone catalyst toward AOR due to the lack of AOR activity (Fig. S3f). The results match those observed in earlier works [43,46,49,66]. As discussed above, the Ni₄Cu₁Co_{1.5}-BP catalyst displays the highest AOR current density and is the focus of the flowing study along with the Ni₄Cu₁-BP catalyst as the control sample.

According to the mechanism of AOR described above, the concentration of OH[−] and NH₃ are two crucial factors in the AOR process. Therefore, the effect of KOH concentration on the AOR of the Ni₄Cu₁Co_{1.5}-BP and Ni₄Cu₁-BP catalysts was first investigated, as displayed in Fig. 2c and S5a. It can be seen that both the Ni₄Cu₁Co_{1.5}-BP and Ni₄Cu₁-BP catalysts demonstrated a negative shift of the onset potential and an increase in the anodic current density with the concentration of KOH from 1 M to 3 M in the AOR. The reason behind the negative shift of the AOR onset potential is that the AOR becomes thermodynamically more favorable at higher KOH concentrations, according to the Nernst Equation [61,67]. Additionally, OH[−] as the reactant can promote the formation of Ni_{1-x-y}Cu_xCo_yOOH and the higher OH[−] concentrations contribute to further oxidation of adsorbed

intermediates, increasing the anodic current density [61,67]. Moreover, as shown in Fig. S5b and c, with increasing KOH concentration, the negative shift of onset potential and the increase of anodic current density are greater in Ni₄Cu₁Co_{1.5}-BP than in Ni₄Cu₁-BP, stemming from the high absorption of OH[−] by Co element.

Afterward, the AOR trend of Ni₄Cu₁Co_{1.5}-BP and Ni₄Cu₁-BP catalysts at different NH₃ concentrations (0–1.0 M) was studied, as shown in Fig. 2d and S6. The anodic current density achieved with the Ni₄Cu₁Co_{1.5}-BP catalyst increases with the rising concentration of NH₃ up to 0.5 M, then it decreases slightly up to 1 M. In contrast, the anodic current density of the Ni₄Cu₁-BP catalyst increases with a rising concentration of NH₃ up to 0.3 M and then decreases slightly. The increase in anodic current density with increasing NH₃ concentration at low-concentration regions is owing to the high availability of NH₃ molecules for the AOR. This process may be governed primarily by NH₃ diffusion. Meanwhile, it may be due to a major kinetics-controlled process, leading to a decrease in the anodic current density at higher NH₃ concentration regions. In the beginning, an increase in NH₃ concentration tends to increase the surface covering of NH₃ molecules on the catalysts, increasing AOR. However, the active site will become saturated when the ammonia concentration attains a certain level. Meanwhile, the high surface covering of ammonia causes a local decrease in OH[−] concentration and influences the diffusion of the reaction products, ultimately inhibiting the AOR [68]. The improved NH₃-saturated activity indicates that Co doping strengthened the acceptability of the Ni₄Cu₁-BP catalyst to the ammonia concentration. This may be because Co has a high affinity for OH[−], which causes the local OH[−] concentration in the catalyst to slowly decrease.

The CVs on Ni₄Cu₁-BP and Ni₄Cu₁Co_{1.5}-BP catalysts at different scan rates were conducted to investigate the behavior of the AOR process and displayed in Fig. S7a and b. The anodic current density of both catalysts increased along with the scanning rates, while the cathodic current density showed an opposite phenomenon. Moreover, a possible diffusion-controlled process in the AOR is suggested by Fig. S7c and d, which show a linear relationship between the anodic or cathodic current density (I_a or I_{cd}) and the square root of the scan rate [44,69,70]. In addition, to eliminate the possible interference of mass transfer problems on the obtained currents, the linear sweep voltammetry (LSV) using a rotating disk electrode technique was utilized to study the AOR process on the catalysts (Fig. S8a and c). As can be seen from Fig. S8b and d, the fitting lines of the Koutecky-Levich (J^{−1} vs. ω^{−1/2}) plots of the Ni₄Cu₁-BP and Ni₄Cu₁Co_{1.5}-BP catalysts at different electrode potentials showed good linearity and parallelism, indicating that the AOR process on the catalysts may be controlled by kinetics [61,71]. From the results in Figs. S7c, d, S8b and d, all the lines displayed nonzero intercepts, confirming that the AOR processes on the Ni₄Cu₁-BP and Ni₄Cu₁Co_{1.5}-BP catalysts are controlled by both diffusion and reaction kinetics [61,72].

As is known to all, the electrocatalytic activity of catalysts depends on the electrochemically active surface area (ECSA). Therefore, the ECSAs of the Ni₄Cu₁-BP and Ni₄Cu₁Co_{1.5}-BP catalysts were compared by measuring the double layer capacitance (C_{dl}) in a non-faradic region at different scan rates, as shown in Fig. S9a and b. The ECSA and C_{dl} can be estimated by the following Equation [73,74]:

$$\text{ECSA} = C_{\text{dl}}/C_s \quad (8)$$

$$i_c = v \cdot C_{\text{dl}} \quad (9)$$

Where C_s, i_c and v denote the specific double-layer capacitance of the sample, the charging current of the double-layer and the scan rate, respectively. According to the report by Trasatti and Petrii [75], many factors such as surface topography (macro- and microroughness), pH, and voltage range can affect the actual C_s value [52,75], leading to the typical value of C_s for Ni-based materials being 22–60 μF cm^{−2} in NaOH and KOH [73,76–79]. Therefore, the estimated ECSA is a relative rather than an absolute value. Consequently, we do not take the actual value of

C_s here but directly compare the ECSA in the Ni_4Cu_1 -BP and $Ni_4Cu_1Co_{1.5}$ -BP catalysts by the C_{dl} obtained from Eq. 8. From Fig. S9c, we can see that the C_{dl} of $Ni_4Cu_1Co_{1.5}$ -BP is 2.04 mF greater than Ni_4Cu_1 -BP (1.85 mF), indirectly indicating that the ECSA of the former is larger than that of the latter, showing the benefits of Co doping.

To further understand the reason for the better performance of $Ni_4Cu_1Co_{1.5}$ -BP catalyst than Ni_4Cu_1 -BP catalyst for AOR, ammonia electro-oxidation experiments on the Ni_4Cu_1 -BP and $Ni_4Cu_1Co_{1.5}$ -BP catalysts were also tested within the temperature range of 25 – 55 °C, employing 1 M KOH with 0.1 M NH_3 as the electrolyte. As observed in Fig. S10a and c, the anodic current density of both catalysts increases with temperatures as expected, because the AOR process is thermally activated [80,81]. Meanwhile, the $Ni_4Cu_1Co_{1.5}$ -BP catalyst always exhibits a higher current density than the Ni_4Cu_1 -BP catalyst at the same temperature, showing better electrocatalytic activity. Fig. S10b and d present the Arrhenius plots for Ni_4Cu_1 -BP and $Ni_4Cu_1Co_{1.5}$ -BP catalysts at various potentials (−0.61 to −0.67 V vs. Hg/HgO), obtained from Fig. S10a and c, respectively. The good liner relationships acquired by plotting $\log(I)$ and $1/T$ from −0.61 to −0.67 V vs. Hg/HgO indicate that the electrode reaction mechanism at this potential range does not change with the increase in temperature [82,83]. In addition, the apparent activation energy (E_a) values can be calculated according to the Arrhenius law using the following Equation [80]:

$$\log I = \log A - \frac{E_a}{2.3R} \left(\frac{1}{T} \right) \quad (10)$$

where I is the measured current, A is the pre-exponential constant, R is the ideal gas constant ($8.314 \text{ J mol}^{-1} \text{ K}^{-1}$), and T is the thermodynamic temperature (K). The potential-dependent apparent activation energies for Ni_4Cu_1 -BP and $Ni_4Cu_1Co_{1.5}$ -BP catalysts are shown in Fig. 2e. At the same potential, the $Ni_4Cu_1Co_{1.5}$ -BP catalyst always displays a lower E_a value than the Ni_4Cu_1 -BP catalyst, which means that the $Ni_4Cu_1Co_{1.5}$ -BP catalyst has higher intrinsic activity, a faster charge transfer process and less energy-consuming [84,85] than the Ni_4Cu_1 -BP catalyst, resulting in better AOR performance.

As a crucial parameter for catalyst applications, the long-term stability of Ni_4Cu_1 -BP and $Ni_4Cu_1Co_{1.5}$ -BP catalysts was also evaluated by CA and CV curves. As depicted in Fig. 2f, both Ni_4Cu_1 -BP and $Ni_4Cu_1Co_{1.5}$ -BP catalysts exhibit higher current densities in the presence of ammonia than in the absence of ammonia, resulting from their AOR activity. Furthermore, in the electrolyte containing ammonia, the CA curves of Ni_4Cu_1 -BP and $Ni_4Cu_1Co_{1.5}$ -BP catalysts dropped rapidly in the first few seconds due to the rapid consumption of local ammonia and OH^- at the initial electrode surface. Afterward, the CA curves slowly decrease to a stable level as the reactions of substances (such as ammonia molecules, OH^- , intermediates and final products) on the electrode surface active site gradually become balanced. Moreover, the current density of the $Ni_4Cu_1Co_{1.5}$ -BP catalyst is much higher than that of the Ni_4Cu_1 -BP catalyst during the whole CA test. When using a higher concentration of electrolyte (3 M KOH + 9 M NH_3), the Ni_4Cu_1 -BP and $Ni_4Cu_1Co_{1.5}$ -BP catalysts also show similar CA test results with good durability (Fig. S11), indicating that they can work stably under the harsh conditions. Besides, as shown in Fig. S12, the maximum anodic current density of $Ni_4Cu_1Co_{1.5}$ -BP catalyst exhibits a small decrease of 3.6 %, whereas the Ni_4Cu_1 -BP catalyst shows a large decrease of 8.5 %, which is more than twice the former. These results confirm that the as-prepared $Ni_4Cu_1Co_{1.5}$ -BP catalyst has outstanding long-term stability for AOR and is superior to as-prepared Ni_4Cu_1 -BP catalyst. This might be owing to the Co doping, which lowered the onset potential of AOR, and then reduced the side reactions (e.g., ammonia overoxidation to nitrites and nitrates) of AOR, resulting in less catalyst degradation [86].

3.3. Investigation of the mechanism

As can be seen in Fig. S13, the AOR activity of both Ni_4Cu_1 -BP and

$Ni_4Cu_1Co_{1.5}$ -BP catalysts was significantly improved after activation, which was consistent with previous work [41] reporting that the activation of NiCu-based catalysts can improve AOR activity. Therefore, it is necessary to activate the anode catalyst electrodes in 3 M KOH prior to the fuel cell test to achieve high AEM-DAFCs performance. On this basis, the changes of the $Ni_4Cu_1Co_{1.5}$ -BP catalyst electrodes before and after activation were investigated. The XRD patterns in Fig. 3a illustrate the structural changes of the $Ni_4Cu_1Co_{1.5}$ -BP catalyst electrodes before and after activation. Before activation, the $Ni_4Cu_1Co_{1.5}$ -BP catalyst electrode showed metallic Ni and Cu phases, consistent with the results in Fig. 1a. In contrast, many of the crystal facets belonging to $Ni(OH)_2$ appear in the activated $Ni_4Cu_1Co_{1.5}$ -BP catalyst electrode. The $Ni(OH)_2$ is then converted into the AOR active compound $NiOOH$. However, the metal Ni peaks are still evident, indicating that only a limited quantity of surface material is oxidized during the activation process. To further study the elemental compositions and chemical states of the $Ni_4Cu_1Co_{1.5}$ -BP catalyst electrode surface before and after activation, X-ray photoelectron spectroscopy (XPS) was carried out. In addition, the XPS spectra of the Ni_4Cu_1 -BP catalyst electrode before activation were characterized to further demonstrate the doping of Co. All the spectra were calibrated with the C 1s signal peak at 284.80 eV, and the Gaussian-Lorentzian method was used in all peak deconvolution and fitting operations. It can be seen from Fig. S14a and d that the Co element was successfully doped into the Ni_4Cu_1 -BP catalyst. Moreover, after the Co doping, the peaks of Ni and Cu were shifted toward lower binding energies (Fig. S14b and d), indicating that part of the electrons from Co were transported to Ni and Cu, resulting in a change of the electronic structure of Ni and Cu and lowering the energy of Ni and Cu 3d-states, which may have changed the adsorption and stabilized certain reaction intermediates [87,88].

As shown in Fig. 3b, the peaks at 852.77 and 870.06 eV for $Ni_4Cu_1Co_{1.5}$ -BP catalyst electrode before activation can be assigned to the $Ni(0) 2p_{3/2}$ and $Ni(0) 2p_{1/2}$ [89], while the peaks at 855.61 and 872.97 eV are ascribed to the $Ni(II) 2p_{3/2}$ and $Ni(II) 2p_{1/2}$ [90], respectively, indicating that a small amount of metallic Ni was oxidized to $Ni(OH)_2$ or NiO on the surface of the as-prepared $Ni_4Cu_1Co_{1.5}$ -BP. After activation, it can be seen that $Ni(III)$ peaks at 856.50 ($Ni 2p_{3/2}$) and 874.08 eV ($Ni 2p_{1/2}$) [91], accompanied by two $Ni(II)$ peaks at 855.29 ($Ni 2p_{3/2}$) and 872.80 eV ($Ni 2p_{1/2}$) [90,92], respectively. Note that after activation, the peak of $Ni(0)$ vanished while $Ni(III)$ peak formed, suggesting that the metallic Ni on the surface of the anode catalytic layer electrode had been oxidized into $Ni(OH)_2$ and $NiOOH$. Similarly, the peaks at 932.61 ($Cu 2p_{3/2}$) and 952.38 eV ($Cu 2p_{1/2}$) of the Cu XPS spectra before activation in Fig. 3c correspond to $Cu(0)$ [90]. After activation, all the $Cu(0)$ has been oxidized to $Cu(II)$, as evidenced by the $Cu(II) 2p_{3/2}$ at a binding energy (BE) of 934.51 eV [90]. In Co XPS spectra (Fig. 3d), the sample before activation exhibits peaks at BEs of 778.07, 793.01, 780.80 and 796.17 eV, which are indexed to $Co(0) 2p_{3/2}$, $Co(0) 2p_{1/2}$, $Co(II) 2p_{3/2}$ and $Co(II) 2p_{1/2}$ [90,91], respectively. For the activated sample, the peaks at 781.37 and 780.10 eV are attributed to the $Co(II) 2p_{3/2}$ and $Co(III) 2p_{3/2}$ [90,93], respectively, showing the presence of $Co(II)$ and $Co(III)$. The absence of $Co(0)$ after activation indicates that $Co(0)$ has been completely converted into $Co(II)$ and $Co(III)$. By comparing XPS results before and after activation, the $Ni(II)$ peak of the latter exhibits a negative shift of 0.32 eV, while the $Co(II)$ peak shows a positive shift of 0.57 eV, accompanied by the appearance of the $Ni(III)$, $Cu(II)$ and $Co(III)$, which may be owing to the formation of $NiCuCo$ hydroxides or oxidized hydroxides ($Ni_{1-x-y}Cu_xCo_yOOH$) after activation. The above XPS results confirmed the formation of $Ni_{1-x-y}Cu_xCo_yOOH$ after the activation of $Ni_4Cu_1Co_{1.5}$ -BP, which, in combination with the significantly improved AOR activity after catalyst activation (Fig. S13), further demonstrated that $Ni_{1-x-y}Cu_xCo_yOOH$ was the dominant active site for AOR in this work. The presence of $NiOOH$, $Cu(OH)_2$ and Co (metal, $Co(OH)_2$, and $CoOOH$) in $Ni_4Cu_1Co_{1.5}$ -BP catalyst electrode revealed by the XPS cannot be observed from its XRD pattern, because the information obtained by

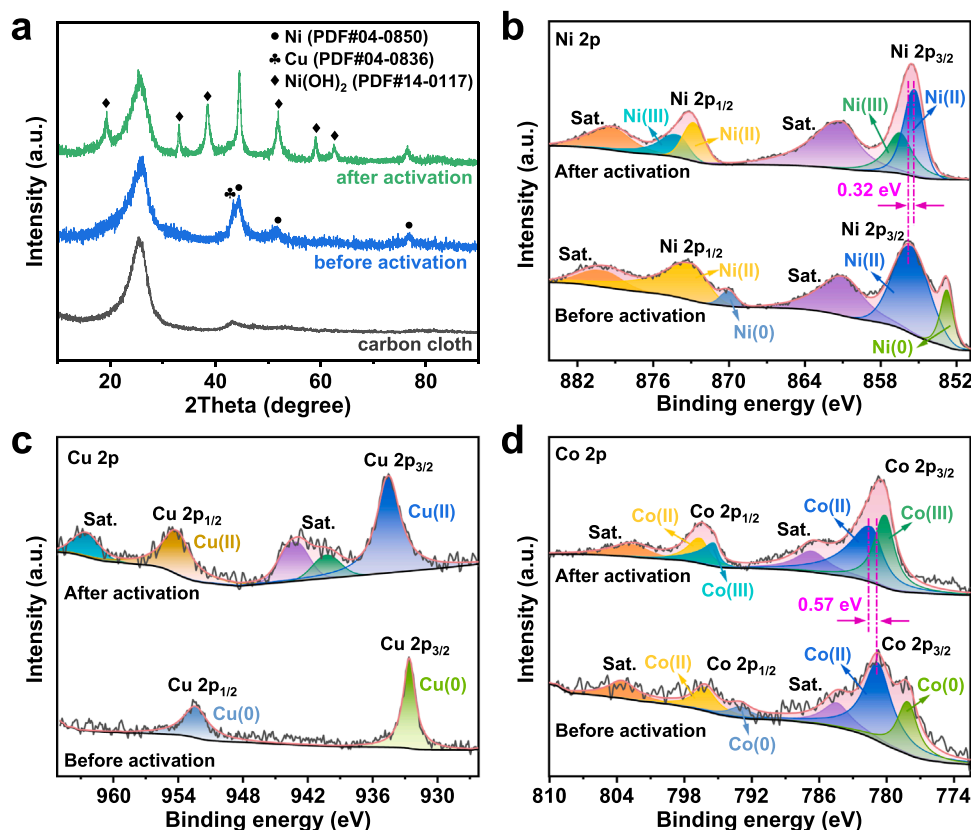


Fig. 3. (a) XRD patterns of carbon cloth, Ni₄Cu₁Co_{1.5}-BP catalyst anode electrode before and after activation. XPS spectra of (b) Ni 2p core level, (c) Cu 2p core level and (d) Co 2p core level for Ni₄Cu₁Co_{1.5}-BP catalyst anode electrode before and after activation.

these two test methods comes from different surface depths of the sample. The different results indicate that the signals of Ni(III), Cu(II) and Co(0, II and III) are exclusively formed on the shallow surface of the sample.

To further gain insights into the catalytic mechanisms, the DFT calculations were first conducted to calculate the Gibbs free energy change (ΔG) for two widely accepted AOR to N₂ mechanisms [94,95], as shown in Table 1. In the Gerischer-Mauerer (G-M) mechanism, the N-N bond will form between intermediates NH_x (x = 1 and 2) and then dehydrogenate to N₂. Noteworthy, there are three possible pathways (N₂H₄, N₂H₃ and N₂H₂ pathways) for AOR in the G-M mechanism, which can be distinguished by *NH₂ to *NH or *H₂NNH₂. As shown in Fig. 4a, the free energy barrier for the formation of *H₂NNH₂ on Ni-Cu-Co-OOH catalyst with N₂H₄ pathway is 0.85 eV, which is lower than that of *NH on Ni-Cu-Co-OOH (1.75 eV) catalyst with N₂H₃ and N₂H₂ pathways. A similar phenomenon can be observed on Ni-Cu-OOH catalyst, where the free energy barrier for the formation of *H₂NNH₂ (0.36 eV) is also lower than the free energy barrier for the formation of *NH (0.90 eV). According to the principle of minimum free energy increase at each step,

Table 1
Two widely accepted AOR mechanisms.

Gerischer-Mauerer (G-M) mechanism[94]	Oswin-Salomon (O-S) mechanism (N + N)[95]
NH ₃ , aq → NH ₃ , ad	NH ₃ , aq → NH ₃ , ad
NH ₃ , ad + OH ⁻ → NH ₂ , ad + H ₂ O + e ⁻	NH ₃ , ad + OH ⁻ → NH ₂ , ad + H ₂ O + e ⁻
NH ₂ , ad + OH ⁻ → NH _{ad} + H ₂ O + e ⁻	NH ₂ , ad + OH ⁻ → NH _{ad} + H ₂ O + e ⁻
NH _x , ad + NH _y , ad → N ₂ H _{x+y} , ad	NH _{ad} + OH ⁻ → N _{ad} + H ₂ O + e ⁻
N ₂ H _{x+y} , ad + (x + y) OH ⁻ → N ₂ + (x + y) H ₂ O + (x + y) e ⁻	N _{ad} + N _{ad} → N ₂
x and y can be 1 or 2.	

the N₂H₄ pathway for the G-M mechanism is energy favorable. Therefore, the rest reaction steps on the N₂H₃ and N₂H₂ pathways will not be considered. In the N + N mechanism, the adsorbed NH₃ dehydrogenates first and then forms the N-N bond between *N. As shown in Fig. 4b, it can be found that the free energy barriers for the N₂ production on Ni-Cu-OOH and Ni-Cu-Co-OOH are 1.33 and 1.75 eV, which are larger than those of Ni-Cu-OOH (1.24 eV) and Ni-Cu-Co-OOH (0.85 eV) performing G-M mechanism with N₂H₄ pathways, respectively. Thus, it can be proposed that Ni-Cu-OOH and Ni-Cu-Co-OOH catalysts will follow the G-M mechanism with the N₂H₄ pathway. Meanwhile, after introducing Co to Ni-Cu-OOH framework, the free energy barrier for the N₂ production decreases by 0.39 eV, leading to enhanced AOR activity.

In addition to the AOR to N₂ pathways discussed above, the possibility of ammonia overoxidation to nitrites and nitrates in Ni-based materials cannot be ignored, since this reaction may affect the AEM-DAFCs performance. Therefore, the pathways of AOR to NO₂⁻ and NO₃⁻ on the Ni-Cu-Co-OOH catalyst were calculated based on previous studies [96,97]. As shown in Fig. S15, the limiting step for both AOR to NO₂⁻ or NO₃⁻ is the formation of *NH₂OH. Compared with the results in Fig. 4a, the key difference between AOR to N₂ and AOR to NO₂⁻ or NO₃⁻ is the formation of *NH₂OH. It can be seen that the free energy barrier for the formation of *NH₂OH (1.10 eV) is lower than that of *NH (1.75 eV), but higher than that of *H₂NNH₂ (0.85 eV). Thus, it will be difficult to generate the NO₂⁻ and NO₃⁻ on the Ni-Cu-Co-OOH catalyst during the AOR. As a result, the Ni-Cu-Co-OOH catalyst still follows the G-M mechanism for AOR to N₂, and the potential determining step is still the formation of *H₂NNH₂.

Furthermore, to understand the origin of activity caused by Co dopants, we calculated the charge density difference and Bader charge. As shown in Fig. 4c, introducing the Co atom caused the charge redistribution. Besides, Bader charge analysis shows that after Co doping, one O atom that bonds with the Cu atom and also serves as the bridge to bind

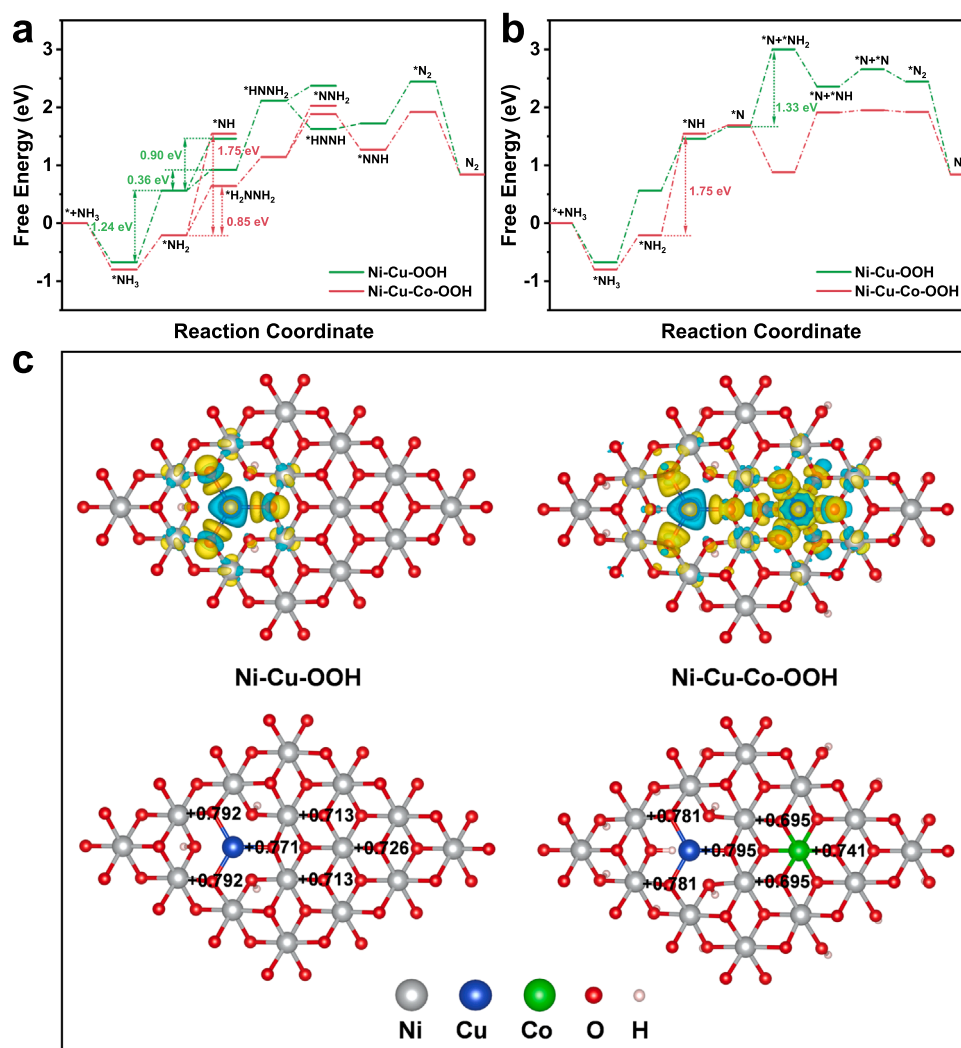


Fig. 4. The Gibbs free energy change diagrams of AOR on Ni-Cu-OOH and Ni-Cu-Co-OOH catalysts toward N_2 under (a) G-M and (b) N + N mechanism, (c) Charge density difference and charge distribution of Ni-Cu-OOH and Ni-Cu-Co-OOH catalysts, where yellow and cyan area indicate the electron accumulation and depletion, respectively, the value of the isosurface is $0.004 \text{ e Bohr}^{-3}$.

the neighboring Ni atom exhibits an obvious increase in electron density, from 0.771 to 0.795 e, while the charge density on the other two O atoms around the Cu atom does not change much, leading to an overall increase in activity. Thus, it can be deduced that the Co atom could induce the charge accumulation around the O site, which contributes to reducing Gibbs free energy of the adsorption, resulting in the enhancement of AOR performance [45].

3.4. Performance of AEM-DAFCs

Here, AEM-DAFCs based on $Ni_4Cu_1Co_x$ ($x = 0, 0.5, 1.0, 1.5$ and 2.0)-BP catalysts anode electrodes were fabricated to explore their performance in AEM-DAFCs. The use of alkaline membranes and the assembly of AEM-DAFCs were the same as reported in our previous work [9]. Meanwhile, Mn-Co-BP2000, a non-noble metal catalyst with superior activity and ammonia tolerance was adopted as the cathodic catalyst in this study which was developed in our previous work [9]. As a result, the AEM-DAFCs based on precious metal-free catalyst electrodes were fabricated.

It is well known that the ammonia concentration in anode fuel plays a crucial role in the performance of AEM-DAFCs. Furthermore, the results of the AOR tests at the RDE level showed that there was an optimal ammonia concentration for the as-synthesized catalysts to achieve the

highest AOR activity. Hence, the AEM-DAFCs with Ni_4Cu_1 -BP and $Ni_4Cu_1Co_{1.5}$ -BP catalysts as anode catalysts were prepared to investigate the effect of ammonia concentration in anode fuel on the performance of AEM-DAFCs. The polarization and power density curves are displayed in Fig. 5a and b, and the corresponding OCV and peak power density (PPD) are listed in Table S2. Notably, when the NH_3 concentration increased from 3 M to 7 M, the PPDs of AEM-DAFCs based on Ni_4Cu_1 -BP or $Ni_4Cu_1Co_{1.5}$ -BP anode catalysts were significantly improved, from 34.4 mW cm^{-2} to 60.0 mW cm^{-2} , and from 66.2 mW cm^{-2} to 115.7 mW cm^{-2} , respectively, resulting from the reduced loss of activation polarization and ohmic polarization. However, with the NH_3 concentration increased to 9 M, the decrease occurred in the PPDs of these AEM-DAFCs. In addition, at the same NH_3 concentration, the performance of AEM-DAFCs based on $Ni_4Cu_1Co_{1.5}$ -BP anode catalyst is better than that based on Ni_4Cu_1 -BP anode catalyst, which further indicates that $Ni_4Cu_1Co_{1.5}$ -BP catalyst is a better AOR catalyst for AEM-DAFCs. Although the NH_3 concentration increased, the OCVs in AEM-DAFCs were almost unchanged. These results are consistent with the results of the AOR half-cell test of the Ni_4Cu_1 -BP and $Ni_4Cu_1Co_{1.5}$ -BP catalysts, where the increase in NH_3 concentration did not affect the onset potential of AOR but changed the anodic current density. From the above results, it is both diffusion and reaction kinetics that control the AOR process on the Ni_4Cu_1 -BP and $Ni_4Cu_1Co_{1.5}$ -BP catalysts. Initially,

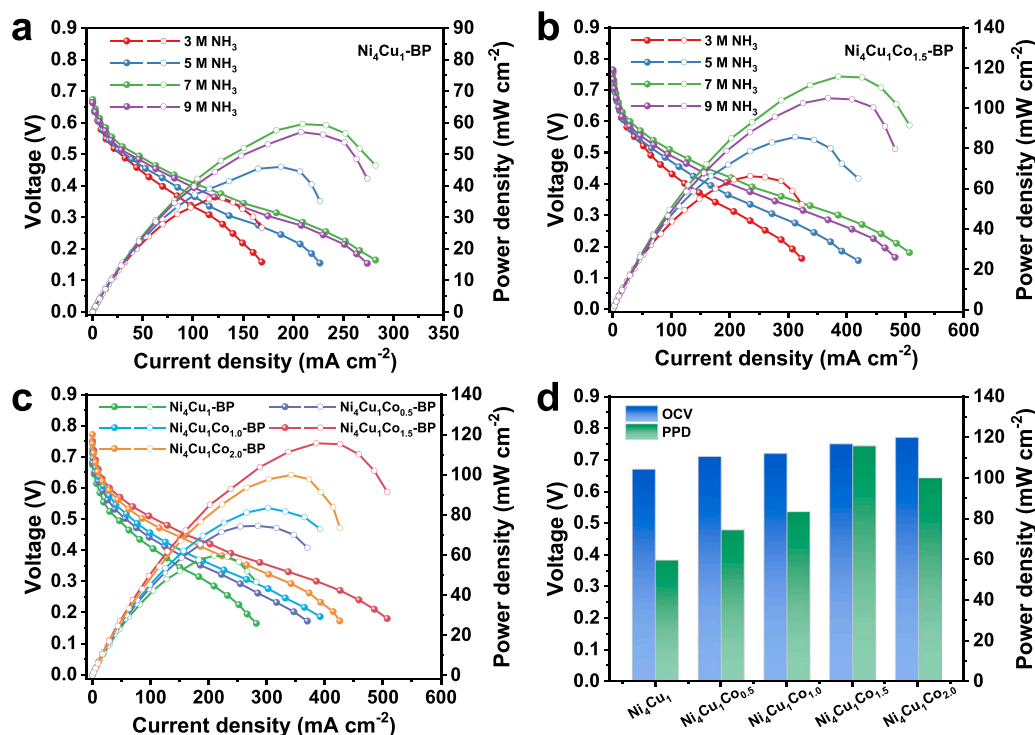


Fig. 5. Polarization and power density curves of AEM-DAFCs based on different anode electrodes: (a) $\text{Ni}_4\text{Cu}_1\text{-BP}$ and (b) $\text{Ni}_4\text{Cu}_1\text{Co}_{1.5}\text{-BP}$ with 3 M KOH containing different concentrations of NH_3 in anode fuels, (c) Polarization and power density curves of AEM-DAFCs based on different anode electrodes from this work with anode fuel of 7 M NH_3 + 3 M KOH, and (d) the corresponding OCV and PPD. Test condition: cell temperature of 80°C , 5 mL min^{-1} anode fuel solution, and 0.2 L min^{-1} pure O_2 with 50 % relative humidity and 200 kPa backpressure.

under the dominant effect of diffusion control, the increase of NH_3 in anode fuel promotes the contact between the anode surface and ammonia, resulting in more active sites participating in AOR and eventually leading to less activation polarization loss. When NH_3 concentration was increased from 7 M to 9 M in anode fuel, the AOR of anode catalysts may be mainly controlled by reaction kinetics. At this time, the active sites of AOR on the anode have reached saturation, and the AOR is affected by the decrease in local OH^- concentration and the difficulty of product diffusion, which leads to a decrease in the AOR and finally increases the activation polarization loss of the DAFCs.

In addition to the ammonia concentration, the effect of Co contents on the performance of the AEM-DAFCs was also investigated. The AEM-DAFCs based on $\text{Ni}_4\text{Cu}_1\text{Co}_{0.5}\text{-BP}$, $\text{Ni}_4\text{Cu}_1\text{Co}_{1.0}\text{-BP}$ and $\text{Ni}_4\text{Cu}_1\text{Co}_{2.0}\text{-BP}$ anode catalysts were fabricated and operated with 7 M NH_3 + 3 M KOH as the anode fuel. The performance of these DAFCs under the same working conditions is shown in Fig. 5c and d with the corresponding

OCVs and PPDs summarized in Table 2. Clearly, the OCV of DAFCs was enhanced by increasing the Co content in the anodic catalyst, from 0.67 V in $\text{Ni}_4\text{Cu}_1\text{-BP}$ to 0.77 V in $\text{Ni}_4\text{Cu}_1\text{Co}_{2.0}\text{-BP}$, indicating that the doping of Co in $\text{Ni}_4\text{Cu}_1\text{-BP}$ anode catalyst was beneficial to improving the OCV of DAFCs. Furthermore, the magnitude order of the OCVs of the DAFCs with as-synthesized catalysts as the anode catalyst is consistent with the magnitude order of the onset potentials obtained from the AOR test in the half-cell (Fig. S4): $\text{Ni}_4\text{Cu}_1\text{Co}_{2.0}\text{-BP} > \text{Ni}_4\text{Cu}_1\text{Co}_{1.5}\text{-BP} > \text{Ni}_4\text{Cu}_1\text{Co}_{1.0}\text{-BP} > \text{Ni}_4\text{Cu}_1\text{Co}_{0.5}\text{-BP} > \text{Ni}_4\text{Cu}_1\text{-BP}$, which confirms that a lower onset overpotential of the AOR will lead to a higher OCV in the DAFCs [24]. Moreover, the PPDs of DAFCs based on as-prepared anode catalysts were 60.0 mW cm^{-2} for $\text{Ni}_4\text{Cu}_1\text{-BP}$, 74.5 mW cm^{-2} for $\text{Ni}_4\text{Cu}_1\text{Co}_{0.5}\text{-BP}$, 83.4 mW cm^{-2} for $\text{Ni}_4\text{Cu}_1\text{Co}_{1.0}\text{-BP}$, 115.7 mW cm^{-2} for $\text{Ni}_4\text{Cu}_1\text{Co}_{1.5}\text{-BP}$ and 99.9 mW cm^{-2} for $\text{Ni}_4\text{Cu}_1\text{Co}_{2.0}\text{-BP}$, respectively. The PPDs order of DAFCs based on $\text{Ni}_4\text{Cu}_1\text{Co}_x$ ($x = 0, 0.5, 1.0, 1.5$ and 2.0) catalysts is also in keeping with the corresponding anodic

Table 2

Comparison of AEM-DAFCs based on nonprecious metal catalysts in the electrodes.

Anode catalysts	Cathode catalysts	Membrane electrolyte	Anode fuels	Temperature ($^\circ\text{C}$)	OCV (V)	PPD (mW cm^{-2})	Refs.
Cr-decorated Ni/C 10 mg cm^{-2}	MnO_2/C 20 mg cm^{-2}	CPPO-PVA	35% NH_3 solution	25	~ 0.85	16	22
NiCu-C 2.5 mg cm^{-2}	$\text{SrCo}_{0.8}\text{Cu}_{0.1}\text{Nb}_{0.1}\text{O}_{3.6}$ 18.67 mg cm^{-2}	FAA	35% NH_3 1 M NaOH	25	~ 0.45	0.25	35
NiCu/C 4.88 mg cm^{-2}	$\alpha\text{-MnO}_2/\text{C}$ 7.87 mg cm^{-2}	PVA-AER	3 M $\text{NH}_3\text{-H}_2\text{O}$	25	0.39	0.35	36
$\text{Ni}_4\text{Cu}_5\text{Fe}_1/\text{C}$ 2.5 mg cm^{-2}	$\text{Ni}_4\text{Cu}_5\text{Fe}_1/\text{C}$ 2.5 mg cm^{-2}	FAA-3-50	7 M $\text{NH}_3\text{-H}_2\text{O}$ 3 M NaOH	80	0.62	8.9	37
$\text{Ni}_4\text{Cu}_1\text{-BP}$ 10 mg cm^{-2}	Mn-Co-BP2000 1.5 mg cm^{-2}	Alkymer® W-211415	7 M NH_3 3 M KOH	80	0.67	60	This work
$\text{Ni}_4\text{Cu}_1\text{Co}_{0.5}\text{-BP}$ 10 mg cm^{-2}					0.71	74.5	
$\text{Ni}_4\text{Cu}_1\text{Co}_{1.0}\text{-BP}$ 10 mg cm^{-2}					0.72	83.4	
$\text{Ni}_4\text{Cu}_1\text{Co}_{1.5}\text{-BP}$ 10 mg cm^{-2}					0.75	115.7	
$\text{Ni}_4\text{Cu}_1\text{Co}_{2.0}\text{-BP}$ 10 mg cm^{-2}					0.77	99.9	

current density order in half-cell AOR measurement (Fig. S4).

A comparison of the AEM-DAFCs with other works based on non-precious metal catalyst electrodes is displayed in Table 2. As can be seen, the Ni-based catalysts were used as the anode catalyst in all of the non-precious metal-based AEM-DAFCs, indicating that the Ni-based catalysts were considered to be the most suitable ones for AOR in DAFCs among non-precious metal catalysts. The PPDs of AEM-DAFCs using the $\text{Ni}_4\text{Cu}_1\text{Co}_x$ ($x = 0, 0.5, 1.0, 1.5$ and 2.0)-BP catalysts prepared in this work as the anode are far greater than those of the others, reflecting the excellent AOR performance of the $\text{Ni}_4\text{Cu}_1\text{Co}_x$ ($x = 0, 0.5, 1.0, 1.5$ and 2.0)-BP catalysts and their better applicability in AEM-DAFCs. The highest PPD (115.7 mW cm^{-2}) in the AEM-DAFCs was obtained when the anode catalyst was $\text{Ni}_4\text{Cu}_1\text{Co}_{1.5}$ -BP. Although this PPD is still lower than that of AEM-DAFCs based on the precious metal anode, it is a great improvement in non-precious metal anodic AEM-DAFCs. Additionally, the inexpensive non-precious metal $\text{Ni}_4\text{Cu}_1\text{Co}_{1.5}$ -BP catalyst is a very competitive anode catalyst in AEM-DAFCs when compared to the cost of the precious metal catalysts.

4. Conclusions

In summary, we have developed a new AOR catalyst by doping Co into Ni_4Cu_1 catalyst through a simple hydrothermal method. The AOR onset potential of $\text{Ni}_4\text{Cu}_1\text{Co}_x$ ($x = 0, 0.5, 1.0, 1.5$ and 2.0) decreases significantly with the increase of Co concentration. Compared with Ni_4Cu_1 -BP, the optimized $\text{Ni}_4\text{Cu}_1\text{Co}_{1.5}$ -BP displays larger electrochemical active surface areas, lower activation energy, and better long-term stability, reflecting the advantages of Co doping. The RDE results show that AOR processes of Ni_4Cu_1 -BP and $\text{Ni}_4\text{Cu}_1\text{Co}_{1.5}$ -BP catalysts are controlled by both diffusion and reaction kinetics. In addition, the DFT calculations reveal that the AOR of Ni_4Cu_1 -BP and $\text{Ni}_4\text{Cu}_1\text{Co}_{1.5}$ -BP catalysts both follow the G-M mechanism, and the doping of Co can raise the electron density surrounding O, allowing it to absorb more intermediates, lower the Gibbs free energy of AOR, and ultimately improve AOR performance. The precious metal-free AEM-DAFC based on the $\text{Ni}_4\text{Cu}_1\text{Co}_{1.5}$ -BP anode and Mn-Co-BP2000 cathode can achieve an OCV of 0.75 V and a PPD of 115.7 mW cm^{-2} . Furthermore, such PPD is the highest in the field of AEM-DAFCs based on precious metal-free electrodes and even comparable to that of Pt-based AEM-DAFCs. These results show that $\text{Ni}_4\text{Cu}_1\text{Co}_{1.5}$ -BP is an excellent non-noble anode catalyst for developing low-temperature AEM-DAFCs with low cost and high performance.

CRediT authorship contribution statement

Zijun Hu: Conceptualization, Methodology, Validation, Formal analysis, Investigation, Data Curation, Writing – Original Draft, Visualization. **Song Lu:** Methodology, Validation, Formal analysis, Investigation, Data Curation, Writing – Original Draft, Visualization. **Fumin Tang:** Formal analysis, Investigation, Data Curation. **Daijun Yang:** Resources, Supervision. **Cunman Zhang:** Resources, Project administration. **Qiangfeng Xiao:** Writing – Review & Editing, Supervision, Project administration, Funding acquisition. **Pingwen Ming:** Writing – Review & Editing, Supervision, Funding acquisition.

Declaration of Competing Interest

The authors declare that they have no known competing financial interests or personal relationships that could have appeared to influence the work reported in this paper.

Data availability

Data will be made available on request.

Acknowledgments

This work was supported by the National Key Research and Development Program of China [No. 2019YFB1504502] and the Fundamental Research Funds for the Central Universities [No. 22120210095].

Appendix A. Supporting information

Supplementary data associated with this article can be found in the online version at doi:10.1016/j.apcatb.2023.122856.

References

- [1] Z. Wan, Y. Tao, J. Shao, Y. Zhang, H. You, Ammonia as an effective hydrogen carrier and a clean fuel for solid oxide fuel cells, *Energy Conv. Manag.* 228 (2021), 113729, <https://doi.org/10.1016/j.enconman.2020.113729>.
- [2] (<https://yearbook.enerdata.net/total-energy/world-consumption-statistics.html>) (accessed 11 January 2023).
- [3] O. Siddiqui, I. Dincer, Development and performance evaluation of a direct ammonia fuel cell stack, *Chem. Eng. Sci.* 200 (2019) 285–293, <https://doi.org/10.1016/j.ces.2019.01.059>.
- [4] W.W. Immerzeel, A.F. Lutz, M. Andrade, A. Bahl, H. Biemans, T. Bolch, S. Hyde, S. Brumby, B.J. Davies, A.C. Elmore, A. Emmer, M. Feng, A. Fernández, U. Haritashya, J.S. Kargel, M. Koppes, P.D.A. Kraaijenbrink, A.V. Kulkarni, P. A. Mayewski, S. Nepal, P. Pacheco, T.H. Painter, F. Pellicciotti, H. Rajaram, S. Rupper, A. Sinisalo, A.B. Shrestha, D. Viviroli, Y. Wada, C. Xiao, T. Yao, J.E. M. Baillie, Importance and vulnerability of the world's water towers, *Nature* 577 (2020) 364–369, <https://doi.org/10.1038/s41586-019-1822-y>.
- [5] IEA, 2023, CO₂ Emissions in 2022, IEA, Paris (<https://www.iea.org/reports/co2-emissions-in-2022>) (accessed 11 March 2023).
- [6] C. Acar, I. Dincer, The potential role of hydrogen as a sustainable transportation fuel to combat global warming, *Int. J. Hydrog. Energy* 45 (2020) 3396–3406, <https://doi.org/10.1016/j.ijhydene.2018.10.149>.
- [7] A.M. Abdalla, S. Hossain, O.B. Nisfindy, A.T. Azad, M. Dawood, A.K. Azad, Hydrogen production, storage, transportation and key challenges with applications: a review, *Energy Conv. Manag.* 165 (2018) 602–627, <https://doi.org/10.1016/j.enconman.2018.03.088>.
- [8] G. Jeerh, M. Zhang, S. Tao, Recent progress in ammonia fuel cells and their potential applications, *J. Mater. Chem. A* 9 (2021) 727–752, <https://doi.org/10.1039/D0TA08810B>.
- [9] Z.J. Hu, Q.F. Xiao, D.D. Xiao, Z.M. Wang, F.K. Gui, Y.K. Lei, J. Ni, D.J. Yang, C. M. Zhang, P.W. Ming, Synthesis of anti-poisoning spinel Mn–Co–C as cathode catalysts for low-temperature anion exchange membrane direct ammonia fuel cells, *ACS Appl. Mater. Interfaces* 13 (2021) 53945–53954, <https://doi.org/10.1021/acsami.1c16251>.
- [10] M. Aziz, A.T. Wijayanta, A.B.D. Nandiyanto, Ammonia as effective hydrogen storage: a review on production, storage and utilization, *Energies* 13 (2020) 3062, <https://doi.org/10.3390/en13123062>.
- [11] U.S. Geological Survey, 2022, Mineral commodity summaries 2022: U.S. Geological Survey, 202 p., <https://doi.org/10.3133/mcs2022>.
- [12] C. Smith, A.K. Hill, L. Torrente-Murciano, Current and future role of Haber-Bosch ammonia in a carbon-free energy landscape, *Energy Environ. Sci.* 13 (2020) 331–344, <https://doi.org/10.1039/c9ee02873k>.
- [13] P.E. Mark Fecke, S. Garner, B. Cox, Review of global regulations for anhydrous ammonia production, use, and storage, *Inst. Chem. Eng. Symp. Ser.* 161 (2016) 1–11, (<https://ammoniaknowhow.com/review-of-global-regulations-for-anhydrous-ammonia-production-use-and-storage-2/>) (accessed 11 January 2023).
- [14] Z. Lyu, J. Fu, T. Tang, J. Zhang, J. Hu, Design of ammonia oxidation electrocatalysts for efficient direct ammonia fuel cells, *Energychem* (2022), 100093, <https://doi.org/10.1016/j.enchem.2022.100093>.
- [15] (<https://www.ammoniaenergy.org/?s=Japan>) (accessed 11 January 2023).
- [16] T. Brown, Japan's Road Map for Fuel Ammonia, (<https://www.ammoniaenergy.org/articles/japans-road-map-for-fuel-ammonia/>) (accessed 11 January 2023).
- [17] T. Brown, US House draft bill defines ammonia as low-carbon fuel, (<https://www.ammoniaenergy.org/?s=US+House+draft+bill+defines+ammonia+as+low-carbon+fuel>) (accessed 11 January 2023).
- [18] T.R. Society, Ammonia: zero-carbon fertiliser, fuel and energy store, (<https://royal.society.org/topics-policy/projects/low-carbon-energy-programme/green-ammonia/>), 2020 (accessed 11 January 2023).
- [19] L. Ding, T. Tang, J.S. Hu, Recent progress in proton-exchange membrane fuel cells based on metal-nitrogen-carbon catalysts, *Acta Phys. -Chim. Sin.* 37 (2021), 2010048, <https://doi.org/10.3866/PKU.WHXB202010048>.
- [20] A.D. Santamaria, M. Mortazavi, Aqueous ammonia wetting of gas-diffusion media for electrochemical cells, *J. Electrochem. Soc.* 167 (2020), 104507, <https://doi.org/10.1149/1945-7111/ab995e>.
- [21] O. Siddiqui, I. Dincer, A review and comparative assessment of direct ammonia fuel cells, *Therm. Sci. Eng. Prog.* 5 (2018) 568–578, <https://doi.org/10.1016/j.tsep.2018.02.011>.
- [22] R. Lan, S. Tao, Direct ammonia alkaline anion-exchange membrane fuel cells, *Electrochem. Solid St.* 13 (2010) B83–B86, <https://doi.org/10.1149/1.3428469>.

- [23] Y. Zhao, B.P. Setzler, J. Wang, J. Nash, T. Wang, B. Xu, Y. Yan, An efficient direct ammonia fuel cell for affordable carbon-neutral transportation, *Joule* 3 (2019) 2472–2484, <https://doi.org/10.1016/j.joule.2019.07.005>.
- [24] B. Achrai, Y. Zhao, T. Wang, G. Tamir, R. Abbasi, B.P. Setzler, M. Page, Y. Yan, S. Gottesfeld, A direct ammonia fuel cell with a KOH-free anode feed generating 180 mW cm⁻² at 120 °C, *J. Electrochem. Soc.* 167 (2020), 134518, <https://doi.org/10.1149/1945-7111/abdd1>.
- [25] Y. Li, H.S. Pillai, T. Wang, S. Hwang, Y. Zhao, Z. Qiao, Q. Mu, S. Karakalos, M. Chen, J. Yang, D. Su, H. Xin, Y. Yan, G. Wu, High-performance ammonia oxidation catalysts for anion-exchange membrane direct ammonia fuel cells, *Environ. Sci.* 14 (2021) 1449–1460, <https://doi.org/10.1039/D0EE03351K>.
- [26] T. Wang, Y. Zhao, B.P. Setzler, Y. Yan, Improving performance and durability of low temperature direct ammonia fuel cells: effect of backpressure and oxygen reduction catalysts, *J. Electrochem. Soc.* 168 (2021), 014507, <https://doi.org/10.1149/1945-7111/abddca>.
- [27] T. Wang, Y. Zhao, B.P. Setzler, R. Abbasi, S. Gottesfeld, Y. Yan, A high-performance 75 W direct ammonia fuel cell stack, *Cell Rep. Phys. Sci.* 3 (2022), 100829, <https://doi.org/10.1016/j.xcrp.2022.100829>.
- [28] G. Jeerh, P. Zou, M. Zhang, S. Tao, Perovskite oxide LaCr_{0.25}Fe_{0.25}Co_{0.5}O_{3-δ} as an efficient non-noble cathode for direct ammonia fuel cells, *Appl. Catal. B: Environ.* 319 (2022), 121919, <https://doi.org/10.1016/j.apcatb.2022.121919>.
- [29] Y. Zhao, T. Wang, B.P. Setzler, R. Abbasi, J. Wang, Y. Yan, A high-performance gas-fed direct ammonia hydroxide exchange membrane fuel cell, *ACS Energy Lett.* 6 (2021) 1996–2002, <https://doi.org/10.1021/acseenergylett.1c00370>.
- [30] G. Jeerh, P. Zou, M. Zhang, S. Tao, Optimization of a perovskite oxide-based cathode catalyst layer on performance of direct ammonia fuel cells, *ACS Appl. Mater. Interfaces* 15 (2023) 1029–1041, <https://doi.org/10.1021/acsaami.2c17253>.
- [31] T. Ioroi, Z. Siroma, S.I. Yamazaki, K. Yasuda, Electrocatalysts for PEM fuel cells, *Adv. Energy Mater.* 9 (2019), 1801284, <https://doi.org/10.1002/aenm.201801284>.
- [32] J.A. Herron, P. Ferrin, M. Mavrikakis, Electrocatalytic oxidation of ammonia on transition-metal surfaces: a first-principles study, *J. Phys. Chem. C* 119 (2015) 14692–14701, <https://doi.org/10.1021/jp512981f>.
- [33] A.C.A. de Vooy, M.T.M. Koper, R.A. van Santen, J.A.R. van Veen, The role of adsorbates in the electrochemical oxidation of ammonia on noble and transition metal electrodes, *J. Electroanal. Chem.* 506 (2001) 127–137, [https://doi.org/10.1016/S0022-0728\(01\)00491-0](https://doi.org/10.1016/S0022-0728(01)00491-0).
- [34] F. Jiao, B. Xu, Electrochemical ammonia synthesis and ammonia fuel cells, *Adv. Mater.* 31 (2018), 1805173, <https://doi.org/10.1002/adma.201805173>.
- [35] P. Zou, S. Chen, R. Lan, S. Tao, Investigation of perovskite oxide SrCo_{0.8}Co_{0.1}Nb_{0.1}O_{3-δ} as a cathode material for room temperature direct ammonia fuel cells, *Chemosuschem* 12 (2019) 2788–2794, <https://doi.org/10.1002/cssc.201900451>.
- [36] M. Zhang, P. Zou, G. Jeerh, S. Chen, J. Shields, H. Wang, S. Tao, Electricity generation from ammonia in landfill leachate by an alkaline membrane fuel cell based on precious-metal-free electrodes, *ACS Sustain. Chem. Eng.* 8 (2020) 12817–12824, <https://doi.org/10.1021/acssuschemeng.0c02926>.
- [37] M. Zhang, J. Zhang, G. Jeerh, P. Zou, B. Sun, M. Walker, K. Xie, S. Tao, A symmetric direct ammonia fuel cell using ternary NiCuFe alloy embedded in a carbon network as electrodes, *J. Mater. Chem. A* 10 (2022) 18701–18713, <https://doi.org/10.1039/D2TA04129D>.
- [38] N.M. Adli, H. Zhang, S. Mukherjee, G. Wu, Review-ammonia oxidation electrocatalysis for hydrogen generation and fuel cells, *J. Electrochem. Soc.* 165 (2018) J3130–J3147, <https://doi.org/10.1149/2.0191815jes>.
- [39] F. Almomani, R. Bhosale, M. Khraishah, A. Kumar, M. Tawalbeh, Electrochemical oxidation of ammonia on nickel oxide nanoparticles, *Int. J. Hydrog. Energy* 45 (2020) 10398–10408, <https://doi.org/10.1016/j.ijhydene.2019.11.071>.
- [40] S. He, Y. Chen, M. Wang, K. Liu, P. Novello, X. Li, S. Zhu, J. Liu, Metal nitride nanosheets enable highly efficient electrochemical oxidation of ammonia, *Nano Energy* 80 (2021), 105528, <https://doi.org/10.1016/j.nanoen.2020.105528>.
- [41] W. Xu, D. Du, R. Lan, J. Humphreys, D.N. Miller, M. Walker, Z. Wu, J.T.S. Irvine, S. Tao, Electrodeposited NiCu bimetal on carbon paper as stable non-noble anode for efficient electrooxidation of ammonia, *Appl. Catal. B: Environ.* 237 (2018) 1101–1109, <https://doi.org/10.1016/j.apcatb.2016.11.003>.
- [42] X. Jiang, D. Ying, X. Liu, M. Liu, S. Zhou, C. Guo, G. Zhao, Y. Wang, J. Jia, Identification of the role of Cu site in Ni–Cu hydroxide for robust and high selective electrochemical ammonia oxidation to nitrite, *Electrochim. Acta* 345 (2020), 136157, <https://doi.org/10.1016/j.electacta.2020.136157>.
- [43] W. Xu, R. Lan, D. Du, J. Humphreys, M. Walker, Z. Wu, H. Wang, S. Tao, Directly growing hierarchical nickel-copper hydroxide nanowires on carbon fibre cloth for efficient electrooxidation of ammonia, *Appl. Catal. B: Environ.* 218 (2017) 470–479, <https://doi.org/10.1016/j.apcatb.2017.07.005>.
- [44] E.T. Sayed, T. Eisa, H.O. Mohamed, M.A. Abdelkareem, A. Allagui, H. Alawadhi, K. Chae, Direct urea fuel cells: challenges and opportunities, *J. Power Sources* 417 (2019) 159–175, <https://doi.org/10.1016/j.jpowsour.2018.12.024>.
- [45] M. Zhu, Y. Yang, S. Xi, C. Diao, Z. Yu, W.S.V. Lee, J. Xue, Deciphering NH₃ adsorption kinetics in ternary Ni–Cu–Fe oxyhydroxide toward efficient ammonia oxidation reaction, *Small* 17 (2021), 2005616, <https://doi.org/10.1002/smll.202005616>.
- [46] Y. Shih, C. Hsu, Kinetics and highly selective N₂ conversion of direct electrochemical ammonia oxidation in an undivided cell using NiCo oxide nanoparticle as the anode and metallic Cu/Ni foam as the cathode, *Chem. Eng. J.* 409 (2021), 128024, <https://doi.org/10.1016/j.cej.2020.128024>.
- [47] R.M. Tesfaye, G. Das, B.J. Park, J. Kim, H.H. Yoon, Ni–Co bimetal decorated carbon nanotube aerogel as an efficient anode catalyst in urea fuel cells, *Sci. Rep.* 9 (2019) 479, <https://doi.org/10.1038/s41598-018-37011-w>.
- [48] R. Ding, L. Qi, M. Jia, H. Wang, Sodium dodecyl sulfate-assisted hydrothermal synthesis of mesoporous nickel cobaltite nanoparticles with enhanced catalytic activity for methanol electrooxidation, *J. Power Sources* 251 (2014) 287–295, <https://doi.org/10.1016/j.jpowsour.2013.11.063>.
- [49] N.A.M. Barakat, M. Motlak, A.A. Elzathary, K.A. Khalil, E.A.M. Abdelghani, Ni_xCo_{1-x} alloy nanoparticle-doped carbon nanofibers as effective non-precious catalyst for ethanol oxidation, *Int. J. Hydrog. Energy* 39 (2014) 305–316, <https://doi.org/10.1016/j.ijhydene.2013.10.061>.
- [50] M.A. Abdelkareem, E.T. Sayed, H.O. Mohamed, M. Obaid, H. Rezk, K. Chae, Nonprecious anodic catalysts for low-molecular-hydrocarbon fuel cells: theoretical consideration and current progress, *Prog. Energy Combust. Sci.* 77 (2020), 100805, <https://doi.org/10.1016/j.pecs.2019.100805>.
- [51] Z.B. Zhuang, S.A. Giles, J. Zheng, G.R. Jenness, S. Caratzoulas, D.G. Vlachos, Y. S. Yan, Nickel supported on nitrogen-doped carbon nanotubes as hydrogen oxidation reaction catalyst in alkaline electrolyte, *Nat. Commun.* 7 (2016), 10141, <https://doi.org/10.1038/ncomms10141>.
- [52] F. Guo, D. Cao, M. Du, K. Ye, G. Wang, W. Zhang, Y. Gao, K. Cheng, Enhancement of direct urea-hydrogen peroxide fuel cell performance by three-dimensional porous nickel-cobalt anode, *J. Power Sources* 307 (2016) 697–704, <https://doi.org/10.1016/j.jpowsour.2016.01.042>.
- [53] G. Kresse, D. Joubert, From ultrasoft pseudopotentials to the projector augmented-wave method, *Phys. Rev. B* 59 (1999) 1758–1775, <https://doi.org/10.1103/PhysRevB.59.1758>.
- [54] G. Kresse, J. Furthmüller, Efficiency of ab-initio total energy calculations for metals and semiconductors using a plane-wave basis set, *Comput. Mater. Sci.* 6 (1996) 15–50, [https://doi.org/10.1016/0927-0256\(96\)00008-0](https://doi.org/10.1016/0927-0256(96)00008-0).
- [55] P.E. Blochl, Projector augmented-wave method, *Phys. Rev. B* 50 (1994) 17953–17979, <https://doi.org/10.1103/physrevb.50.17953>.
- [56] J.P. Perdew, K. Burke, E. Matthias, Generalized gradient approximation made simple, *Phys. Rev. Lett.* 77 (1996) 3865–3868, <https://doi.org/10.1103/PhysRevLett.77.3865>.
- [57] J.P. Perdew, M. Ernzerhof, K. Burke, Rationale for mixing exact exchange with density functional approximations, *J. Chem. Phys.* 105 (1996) 9982–9985, <https://doi.org/10.1063/1.472933>.
- [58] S. Grimme, J. Antony, S. Ehrlich, H. Krieg, A consistent and accurate ab initio parametrization of density functional dispersion correction (DFT-D) for the 94 elements H–Pu, *J. Chem. Phys.* 132 (2010), 154104, <https://doi.org/10.1063/1.3382344>.
- [59] J.K. Nørskov, J. Rossmeisl, A. Logadottir, L. Lindqvist, J.R. Kitchin, T. Bligaard, H. Jonsson, Origin of the overpotential for oxygen reduction at a fuel-cell cathode, *J. Phys. Chem. B* 108 (2004) 17886–17892, <https://doi.org/10.1021/jp047349j>.
- [60] Z.J. Hu, D. Chen, P. Yang, L.J. Yang, L.S. Qin, Y.X. Huang, X.C. Zhao, Sol-gel-processed yttrium-doped NiO as hole transport layer in inverted perovskite solar cells for enhanced performance, *Appl. Surf. Sci.* 441 (2018) 258–264, <https://doi.org/10.1016/j.apsusc.2018.01.236>.
- [61] V. Vedharathnam, G.G. Botte, Understanding the electro-catalytic oxidation mechanism of urea on nickel electrodes in alkaline medium, *Electrochim. Acta* 81 (2012) 292–300, <https://doi.org/10.1016/j.electacta.2012.07.007>.
- [62] F. Almomani, M. Ali, H. Salah Saad, Electrochemical oxidation of ammonia (NH₄⁺/NH₃) on synthesized nickel-cobalt oxide catalyst, *Int. J. Hydrog. Energy* 46 (2021) 4678–4690, <https://doi.org/10.1016/j.ijhydene.2020.03.094>.
- [63] A. Kapalka, A. Cally, S. Neodo, C. Cominell, M. Wächter, K.M. Udert, Electrochemical behavior of ammonia at Ni/Ni(OH)₂ electrode, *Electrochim. Commun.* 12 (2010) 18–21, <https://doi.org/10.1016/j.elecom.2009.10.026>.
- [64] M. Blasco-Ahicart, J. Soriano-López, J.J. Carbó, J.M. Poblet, J.R. Galan-Mascaros, Polyoxometalate electrocatalysts based on earth-abundant metals for efficient water oxidation in acidic media, *Nat. Chem.* 10 (2018) 24–30, <https://doi.org/10.1038/nchem.2874>.
- [65] G. de Falco, M. Florent, A. De Rosa, T.J. Bandosz, Proposing an unbiased oxygen reduction reaction onset potential determination by using a Savitzky-Golay differentiation procedure, *J. Colloid Interfaces. Sci.* 586 (2021) 597–600, <https://doi.org/10.1016/j.jcis.2020.10.127>.
- [66] E.T. Sayed, M.A. Abdelkareem, H. Alawadhi, A.G. Olabi, Enhancing the performance of direct urea fuel cells using Co dendrites, *Appl. Surf. Sci.* 555 (2021), 149698, <https://doi.org/10.1016/j.apsusc.2021.149698>.
- [67] W. Wang, D. Chai, J. Zhang, S. Xue, Y. Wang, Z. Lei, Ni₅Sm–P/C ternary alloyed catalyst as highly efficient electrocatalyst for urea electrooxidation, *J. Taiwan Inst. Chem. Eng.* 80 (2017) 326–332, <https://doi.org/10.1016/j.jtice.2017.07.017>.
- [68] Z. Li, Y. Wang, G.G. Botte, Revisiting the electrochemical oxidation of ammonia on carbon-supported metal nanoparticle catalysts, *Electrochim. Acta* 228 (2017) 351–360, <https://doi.org/10.1016/j.electacta.2017.01.020>.
- [69] M.A. Shenashen, D. Hassen, S.A. El-Safty, H. Isago, A. Elmarakbi, H. Yamaguchi, Axially oriented tubercle vein and X-crossed sheet of Ni–Co₃O₄@C hierarchical mesoarchitectures as potential heterogeneous catalysts for methanol oxidation reaction, *Chem. Eng. J.* 313 (2017) 83–98, <https://doi.org/10.1016/j.cej.2016.12.003>.
- [70] Y. Kang, W. Wang, J. Li, Q. Li, S. Liu, Z. Lei, A highly efficient Pt–NiO/C electrocatalyst for ammonia electro-oxidation, *J. Electrochem. Soc.* 164 (2017) F958–F965, <https://doi.org/10.1149/2.1051709jes>.
- [71] M. Gonzalez-Reyna, M.S. Luna-Martinez, J.F. Perez-Robles, Nickel supported on carbon nanotubes and carbon nanospheres for ammonia oxidation reaction, *Nanotechnology* 31 (2020), 235706, <https://doi.org/10.1088/1361-6528/ab73b6>.

- [72] N.W. Maxakato, K.I. Ozoemena, C.J. Arendse, Dynamics of electrocatalytic oxidation of ethylene glycol, methanol and formic acid at MWCNT platform electrochemically modified with Pt/Ru nanoparticles, *Electroanalysis* 22 (2010) 519–529, <https://doi.org/10.1002/elan.200900397>.
- [73] C.C.L. McCrory, S. Jung, J.C. Peters, T.F. Jaramillo, Benchmarking heterogeneous electrocatalysts for the oxygen evolution reaction, *J. Am. Chem. Soc.* 135 (2013) 16977–16987, <https://doi.org/10.1021/ja407115p>.
- [74] Y. Wang, G. Liu, Reduced graphene oxide supported nickel tungstate nano-composite electrocatalyst for anodic urea oxidation reaction in direct urea fuel cell, *Int. J. Hydrog. Energy* 45 (2020) 33500–33511, <https://doi.org/10.1016/j.ijhydene.2020.09.095>.
- [75] S. Trasatti, O.A. Petrii, Real surface area measurements in electrochemistry, *J. Electroanal. Chem.* 327 (1992) 353–376, [https://doi.org/10.1016/0022-0728\(92\)80162-W](https://doi.org/10.1016/0022-0728(92)80162-W).
- [76] J.L. Weininger, M.W. Breiter, Hydrogen evolution and surface oxidation of nickel electrodes in alkaline solution, *J. Electrochem. Soc.* 111 (1964) 707, <https://doi.org/10.1149/1.2426216>.
- [77] A. Lasia, A. Rami, Kinetics of hydrogen evolution on nickel electrodes, *J. Electroanal. Chem.* 294 (1990) 123–141, [https://doi.org/10.1016/0022-0728\(90\)87140-F](https://doi.org/10.1016/0022-0728(90)87140-F).
- [78] P. Gu, L. Bai, L. Gao, R. Brousseau, B.E. Conway, Problems in the determination of adsorption behaviour of intermediates in faradaic reactions: distinction between double layer and adsorption capacitance of electrocatalysts determined from fast potential relaxation transients, *Electrochim. Acta* 37 (1992) 2145–2154, [https://doi.org/10.1016/0013-4686\(92\)85105-T](https://doi.org/10.1016/0013-4686(92)85105-T).
- [79] M.W. Louie, A.T. Bell, An investigation of thin-film Ni-Fe oxide catalysts for the electrochemical evolution of oxygen, *J. Am. Chem. Soc.* 135 (2013) 12329–12337, <https://doi.org/10.1021/ja405351s>.
- [80] A. Velázquez-Palenzuela, F. Centellas, J.A. Garrido, C. Arias, R.M. Rodríguez, E. Brillas, P. Cabot, Kinetic analysis of carbon monoxide and methanol oxidation on high performance carbon-supported Pt–Ru electrocatalyst for direct methanol fuel cells, *J. Power Sources* 196 (2011) 3503–3512, <https://doi.org/10.1016/j.jpowsour.2010.12.044>.
- [81] W. Wang, Y. Yang, Y. Liu, Z. Zhang, W. Dong, Z. Lei, Hybrid NiCoO_x adjacent to Pd nanoparticles as a synergistic electrocatalyst for ethanol oxidation, *J. Power Sources* 273 (2015) 631–637, <https://doi.org/10.1016/j.jpowsour.2014.09.120>.
- [82] E. Habibi, H. Razmi, Kinetics of direct ethanol fuel cell based on Pt-PoPD nano particle anode catalyst, *Int. J. Hydrog. Energy* 38 (2013) 5442–5448, <https://doi.org/10.1016/j.ijhydene.2012.09.079>.
- [83] A. Dutta, A. Mondal, J. Datta, Tuning of platinum nano-particles by Au usage in their binary alloy for direct ethanol fuel cell: controlled synthesis, electrode kinetics and mechanistic interpretation, *J. Power Sources* 283 (2015) 104–114, <https://doi.org/10.1016/j.jpowsour.2015.01.113>.
- [84] Y. Wang, T.S. Nguyen, X. Liu, X. Wang, Novel palladium–lead (Pd–Pb/C) bimetallic catalysts for electrooxidation of ethanol in alkaline media, *J. Power Sources* 195 (2010) 2619–2622, <https://doi.org/10.1016/j.jpowsour.2009.11.072>.
- [85] Y. Yang, W. Wang, Y. Liu, F. Wang, D. Chai, Z. Lei, Pd nanoparticles supported on phenanthroline modified carbon as high active electrocatalyst for ethylene glycol oxidation, *Electrochim. Acta* 154 (2015) 1–8, <https://doi.org/10.1016/j.electacta.2014.12.072>.
- [86] J.J. Medvedev, Y. Tobolovskaya, X.V. Medvedeva, S.W. Tatarchuk, F. Li, A. Klinkova, Pathways of ammonia electrooxidation on nickel hydroxide anodes and an alternative route towards recycled fertilizers, *Green Chem.* 24 (2022) 1578–1589, <https://doi.org/10.1039/d1gc04140a>.
- [87] S.W. Tatarchuk, R.M. Choueiri, X.V. Medvedeva, L.D. Chen, A. Klinkova, Inductive effects in cobalt-doped nickel hydroxide electronic structure facilitating urea electrooxidation, *Chemosphere* 279 (2021), 130550, <https://doi.org/10.1016/j.chemosphere.2021.130550>.
- [88] X.D. Yan, Q.T. Hu, G.H. Wang, W.D. Zhang, J.Y. Liu, T. Li, Z.G. Gu, NiCo layered double hydroxide/hydroxide nanosheet heterostructures for highly efficient electro-oxidation of urea, *Int. J. Hydrog. Energy* 45 (2020) 19206–19213, <https://doi.org/10.1016/j.ijhydene.2020.05.052>.
- [89] C.E. Dube, B. Workie, S.P. Kounaves, A.J. Robbat, M.L. Aksu, G. Davies, Electrodeposition of metal alloy and mixed oxide films using a single-precursor tetranuclear copper-nickel complex, *J. Electrochem. Soc.* 142 (1995) 3357–3365, <https://doi.org/10.1149/1.2049987>.
- [90] N.S. McIntyre, M.G. Cook, X-Ray photoelectron studies on of cobalt, nickel, and copper, *Anal. Chem.* 47 (1975) 2208–2213, <https://doi.org/10.1021/ac60363a034>.
- [91] M.C. Biesinger, B.P. Payne, A.P. Grosvenor, L.W.M. Lau, A.R. Gerson, R.S.C. Smart, Resolving surface chemical states in XPS analysis of first row transition metals, oxides and hydroxides: Cr, Mn, Fe, Co and Ni, *Appl. Surf. Sci.* 257 (2011) 2717–2730, <https://doi.org/10.1016/j.apsusc.2010.10.051>.
- [92] R.T. Gao, D. He, L. Wu, K. Hu, X. Liu, Y. Su, L. Wang, Towards long-term photostability of nickel hydroxide/BiVO₄ photoanodes for oxygen evolution catalysts via in situ catalyst tuning, *Angew. Chem. Int. Ed.* 59 (2020) 6213–6218, <https://doi.org/10.1002/anie.201915671>.
- [93] S. Liu, D. Ni, H. Li, K.N. Hui, C. Ouyang, S.C. Jun, Effect of cation substitution on the pseudocapacitive performance of spinel cobaltite MCo₂O₄ (M = Mn, Ni, Cu, and Co) dagger, *J. Mater. Chem. A* 6 (2018) 10674–10685, <https://doi.org/10.1039/c8ta00540k>.
- [94] H. Gerischer, A. Mauerner, Untersuchungen zur anodischen oxidation von ammoniak an platin-elektroden, *J. Electroanal. Chem.* 25 (1970) 421–433, [https://doi.org/10.1016/S0022-0728\(70\)80103-6](https://doi.org/10.1016/S0022-0728(70)80103-6).
- [95] H.G. Oswin, M. Salomon, The anodic oxidation of ammonia at platinum black electrodes in aqueous KOH electrolyte, *Can. J. Chem.* 41 (1963) 1686–1694, <https://doi.org/10.1139/v63-243>.
- [96] R.M. Choueiri, L.D. Chen, Favorable electrocatalytic ammonia oxidation reaction thermodynamics on the β -NiOOH(0001) surface computed by density functional theory, *J. Phys. Chem. C* 126 (2022) 17952–17965, <https://doi.org/10.1021/acs.jpcc.2c06174>.
- [97] R.M. Choueiri, S.W. Tatarchuk, A. Klinkova, L.D. Chen, Mechanism of ammonia oxidation to dinitrogen, nitrite, and nitrate on β -Ni(OH)₂ from first-principles simulations, *Electrochem. Sci. Adv.* 2 (2022), 2100142, <https://doi.org/10.1002/elsa.202100142>.